Concrete behaviour against high velocity impacts

Miguel Filipe Lopes Chambino

Dissertation submitted in partial fulfilment of the requirements for the degree of

Master of Science in **Military Engineering**

Adviser: Lieutenant-Colonel David Lecompte

Co-adviser: Professor Doutor Hugo Miguel Bento Rebelo

Examination Committee

Chairperson: Prof. Dr. Paula Manuela Dos Santos Lopes Do Rego Figueiredo

Supervisor: Lieutenant-Colonel David Lecompte

Members of the Committee: Prof. Dr. Filipe Santos

Members of the Committee: Lieutenant-Colonel Pedro José Da Silva Gonçalves Matias

November 2023

Statement

I declare that this document is an original work of my authorship and that it complies with all the requirements of the Code of Conduct and Good Practices of the Military Academy and the University of Lisbon.

Acknowledgments

To my parents and brother, for the quality education they gave me, for the direct transmission of values, for their unceasing pursuit of my well-being and, above all, for all the self-sacrifice they underwent for the sake of my education in particular and my future in general.

To my girlfriend, Catarina, for always being there for me and supporting me unconditionally in everything. For keeping me focused and aiding me in improving and achieving the best possible work. My deepest thanks to her.

To Lieutenant Colonel David Lecompte, my scientific advisor, for the reception in Belgium and guidance throughout this project. I appreciate the availability, support, valuable advice, and dedication, both technically and personally, to my work.

To Bachir Belkassem and George Kechagiadakis, I extend my heartfelt gratitude for your consistent engagement with valuable ideas and suggestions. Your collaborative spirit was instrumental in my progress, motivating me to aim higher.

My profound gratitude to Professor Hugo Rebelo, whose essential contributions significantly influenced the outcomes of the numerical models. The collaborative exchange of ideas and his unwavering support played an instrumental role in enhancing this dissertation.

My greatest thanks to Cap Eng João Conceição for enabling my involvement in this project, consistently offering assistance and contributing to the excellence of this dissertation.

I thank Lieutenant Colonel of Military Engineering Pedro Matias, my gratitude for the opportunity offered to me, having made himself available to establish the links that make this exchange to the Royal Military Academy possible.

To the FOXTROT class of 16/17 and 17/18 for all the camaraderie over these seven years, without you this path would not have been the same, thank you, comrades.

To my military engineering class, if I made it to this final stage of the course, it was undoubtedly because of all the help and support they gave me. Special thanks to Tiago Ferreira and Antonio Lima for their help and support with this dissertation.

To all the team in Centre of Competence for infrastructure Protection (CCIP), to Cap Eng Matos, to First Sargent Eng Nobre, and to all the present from Heavy Combat Engineering Company making possible also the experimental field tests.

Resumo

É cada vez mais frequente testemunhar ações extremas, sejam de origem natural ou humana, tais como explosões ou impactos. O terrorismo, a guerra ou ações acidentais desta tipologia originam, normalmente, consequências catastróficas, particularmente em infraestruturas críticas.

Neste sentido, urge o estudo de soluções protetivas capazes de mitigar o dano em infraestruturas críticas, preservando desta forma a vida humana. Ainda neste âmbito, o estudo do betão face a ações extremas como a explosão ou impactos de alta velocidade torna-se vital.

A presente dissertação desenvolve-se no âmbito do projeto de investigação intitulado "Proteção de Infraestruturas Sujeitas a Ações Extremas (PrISAEx)", financiado pelo Centro de Investigação, Desenvolvimento e Inovação da Academia Militar (CINAMIL), tendo como principal objetivo estudar o comportamento do betão sujeito a impactos de alta velocidade, de forma a contribuir para a conceção e dimensionamento de soluções protetivas que melhorem o comportamento do betão face a esta ação.

Este estudo analisa o comportamento de blocos de betão sujeitos a impactos de alta velocidade (>1000 m/s), originados por um *Explosively Formed Penetrator* (EFP). Para tal, foi realizada uma análise numérica com recurso ao programa LS-DYNA, de forma a analisar os mecanismos de rotura do betão. Posteriormente, os resultados numéricos foram comparados e validados com oito testes experimentais.

Numa primeira fase, foi desenvolvido um modelo numérico bidimensional (2D) axisimétrico de um EFP para capturar o seu processo de formação e características fundamentais. Após constatar que o EFP atingiria a velocidade desejada, foi realizada uma campanha experimental com dois tipos de blocos de betão, um com agregado de basalto e outro com agregado de calcário. Posteriormente, foi criado um modelo tridimensional (3D), permitindo uma simulação mais realista do impacto do EFP contra um bloco de betão. Este modelo possibilitou uma avaliação mais precisa do desempenho do EFP e da sua interação com o bloco de betão. Por fim, a profundidade de penetração, fragmentação e a dinâmica global do impacto foram analisadas e comparadas com os resultados experimentais.

Através deste estudo, foi possível constatar que agregados mais resistentes demonstraram uma melhor capacidade de dissipação de energia, evidenciada pela menor penetração. Além disso, observamos a confirmação dos diferentes mecanismos de ruptura descritos na literatura tendo como objetivo contribuir futuramente para o desenvolvimento de soluções protetivas visando a mitigação desses efeitos. De destaque, a relevância da modelação numérica, uma vez que os resultados se aproximaram dos valores reais.

Palavras-chave: Alta Velocidade; Modelação numérica; Impacto; Comportamento dinâmico.

Abstract

Today, it is increasingly common to witness extreme events, whether of natural or human origin, such as explosions or impacts. Terrorism, warfare, or accidental incidents of this kind usually result in catastrophic consequences, particularly for critical infrastructure.

In this context, there is an urgent need to study protective solutions that can minimize damage to critical infrastructure, thereby safeguarding human lives. Furthermore, within this context, investigating how concrete responds to extreme events like explosions or high-speed impacts is of paramount importance.

This dissertation is developed within the research project entitled 'Protection of Infrastructures Subjected to Extreme Actions (PrISAEx),' funded by the Research, Development, and Innovation Centre of the Military Academy (CINAMIL). Its main objective is to study the behaviour of concrete subjected to high-speed impacts to contribute to the design and dimensioning of protective solutions that improve the concrete's behaviour against these events.

This study examines the behaviour of concrete blocks subjected to high-speed impacts (>1000 m/s) generated by an Explosively Formed Penetrator (EFP). For this purpose, an experimental campaign was conducted in combination with a numerical analysis that resorted to the LS-DYNA finite element software in order to analyse the concrete fracture mechanisms. Subsequently, the numerical results were compared and validated with eight experimental tests.

In the initial phase, a two-dimensional (2D) axisymmetric numerical model of an EFP was developed to capture its formation process and fundamental characteristics. After confirming that the EFP would achieve the desired speed, an experimental campaign was conducted using two types of concrete blocks, one with basalt aggregate and the other with limestone aggregate. Subsequently, a three-dimensional (3D) model was created, allowing for a more realistic simulation of the EFP's impact on a concrete block. This model enabled a more precise assessment of the EFP's performance and its interaction with the concrete block. Finally, penetration depth, fragmentation, and overall impact dynamics were analysed and compared with the experimental results.

Through this study, it was possible to observe that harder aggregates demonstrated improved energy dissipation capabilities, as evidenced by reduced penetration. Furthermore, we confirmed the existence of various fracture mechanisms as described in the literature, with the aim of contributing to the future development of protective solutions to mitigate these effects. Notably, the importance of numerical modeling was highlighted, as the results closely approximated real-world values.

Keywords: High Velocity; Numerical Modelling; Impact; Dynamic Behaviour.

Table of Contents

Table of figures

Table of tables

List of abbreviations and acronyms

2D	Two dimensional
3D	Three dimensional
AEPW	Advanced Earth Penetration Weapons
ALE	Arbitrary Lagrangian-Eulerian
AP	Armour piercing
CCPI	Centre of Competence for infrastructure Protection
CINAMIL	Centro de Investigação, Desenvolvimento e Inovação da Academia Militar
CNC	Computer numerical control
DIF	Dynamic increase factor
EOS	Equation of state
EOD	Explosive Ordnance Disposal
EFP	Explosively formed projectile
FE	Finite element
IED's	Improvised Explosive Devices
JWL	Jones-Wilkins-Lee
LSTC	Livermore Software Technology Corporation
KCC	Karagozian and Case Concrete
NDRC	National Defense Research Committee
PET	Polyethylene terephthalate
PETG	Polyethylene terephthalate glycol-modified
PrISAEx	Proteção de Infraestruturas Sujeitas a Ações Extremas
RHA	Rolled Homogeneous Armor
UFC	Unified facilities criteria
VOD	Velocities of detonation

Nomenclature

Latin nomenclature

A	Cross-sectional area of the penetrator
A_p	Weight of the missile
C	Charge weight
d	Diameter of the projectile
E_s	Young's modulus of steel
E	Young's modulus of the missile material
E	Specific explosive kinetic energy of the explosive used
f_c'	Concrete compressive strength
k_p	Penetration factor for reinforced concrete
K	Penetrability factor
M	Projectile weight
N^*	Missile shape factor
v_0	Striking velocity
w	Weight of the projectile
x	Penetration depth

Greek nomenclature

ε	Strain
α	Thermal expansion coefficient
λ	Thermal conductivity
ν	Poisson's ratio
ρ	Mass density
σ	Stress

1. Introduction

1.1 Context and problem definition

From ancient times to modern days, defence has been a key function of construction, as seen in the construction of medieval castles and contemporary fortifications. In today's world, where the threat of terrorism or accidental explosions is on the rise, there is a growing need to design large civil buildings such as offices, airports, and public structures that are able to withstand various events and ensure the safety of its occupants.

Whether they arise naturally or are caused by human activities, extreme events that impact infrastructure, including explosions, impacts, and natural disasters, have increasingly captured the attention of the public. There is a growing interest in assessing their effects on structures and mitigating their consequences, which may be devastating.

Terrorist attacks, for many years, and more recently war, have been a persistent threat to security across the globe. Additionally, the rise of extremist groups, coupled with the availability of advanced technology and weaponry, has resulted in increasingly sophisticated and deadly attacks. These attacks often involve the use of explosives, whose impact can be devastating, particularly when aimed at infrastructure such as embassies, buildings, bridges, hospitals, military general headquarters and other critical structures [1]. Therefore, it is crucial to consider the resilience and resistance of these structures to withstand such extreme events and protect the lives of the people relying on them.

Regarding high-velocity impacts, it is essential to investigate the behaviour of materials when subjected to such phenomena. Concrete, being a commonly used construction material due to its structural capacity and cost-effectiveness, deserves particular attention in these studies. Its widespread application includes the construction of protective structural components and critical infrastructure. [2]

High-velocity impacts involve extreme forces and energy transfer, causing significant damage to structures. The speed and mass of the projectile, as well as the material properties and structural characteristics of the target, play crucial roles in determining the outcome of such events. Advanced acceleration techniques, such as two- or three-staged light gas guns, plasma accelerators, and shaped charges, have found extensive application in the field of high-velocity impact research [3]. Researchers and engineers have been conducting extensive studies to investigate the response of materials to high-velocity impacts [4-6]. These studies involve experimental tests, numerical simulations, and theoretical analyses to gain insights into the complex physics involved.

Experimental tests employ gas guns or explosive-driven launchers to propel projectiles at high velocities toward target materials. These tests allow researchers to observe the damage mechanisms, deformation patterns, and penetration depths caused by the impacts. They also provide valuable data for validating numerical models and developing predictive capabilities.

Numerical simulations, such as finite element analysis, have become indispensable tools in studying high-velocity impacts. These simulations involve complex algorithms that model the behavior of materials, considering factors like material strength, strain rate sensitivity, and fracture properties. by inputting the projectile parameters, target material properties, and impact conditions, numerical simulations can predict the response of structures and aid in the design of protective systems.

The knowledge gained from these research efforts is invaluable for enhancing the safety and resilience of structures against terrorist attacks and accidental explosions. It informs the development of advanced protective systems, innovative materials, and design guidelines that can mitigate the destructive effects of high-velocity impacts.

1.2 Motivation and objectives

This master's dissertation is both a personal and professional challenge and will be carried out in the military context, considering that it will certainly be an asset to the Portuguese Army. The possibility of being able to integrate and promote some kind of scientific and technological advance for the Portuguese Army was undoubtedly one of my main sources of motivation.

The issue described in the preceding section has increasingly come under the spotlight, providing the impetus for the initiation of this dissertation. The present dissertation focuses on the study of concrete behaviour when subjected to high-velocity impacts. This work aims to contribute to the development of knowledge in this specific area, which still lacks research due to its complexity and the challenges associated with conducting full-scale tests.

To achieve this objective, the plan involves conducting numerical studies, designing and the execution of full-scale field tests involving high-velocity impacts on concrete blocks. For this study it was used explosively formed projectiles (EFP) as an accelerator to achieve higher velocities greater than 1000 m/s [7], in order to evaluate concrete damage.

Understanding the behaviour of concrete under dynamic loading is crucial for designing resilient structures for extreme events, such as earthquakes, explosions, and high-speed impacts. By improving our understanding of the behaviour of concrete under dynamic loading, we can develop more effective and efficient materials and structures capable of withstanding extreme events and minimizing the risk of catastrophic failure.

1.3 Dissertation outline

This chapter describes the organization of the dissertation.

Chapter 1, Introduction: In this chapter, we will establish the groundwork for high-velocity impacts. It also covers the motivation and objectives of the work to be carried out.

Chapter 2, Literature Review: This chapter aims to cover all the relevant state-of-the-art on the behaviour of concrete against impacts, failure mechanisms of concrete, introduction to high-velocity impacts, equations used and previously conducted experimental and numerical.

Chapter 3, Numerical Design of the EFP: This chapter introduces the finite element program which was used and then explained the model that was made to see if the EFP design would reach the required speed.

Chapter 4, Experimental Campaign: This chapter discusses the entire experimental campaign, which is divided into two main sub-topics, the first representing all the equipment used and the entire thought process to carry out the experimental campaign, and the second sub-topic presenting the experimental results.

Chapter 5, Numerical Model Study: This chapter introduces the numerical model developed to replicate the conditions of the experimental campaign. The primary goal is to validate the experimental campaign results while also obtaining additional data that might have been challenging to measure during the tests.

Chapter 5, Conclusions: The aim of this chapter is to draw conclusions from the work carried out and proposals for future work.

1.4 Dissertation outcomes

During the development of this work, the author published the following scientific works:

Presentation at international conferences

- Chambino, M., et al. (2023). Numerical simulation of high-velocity impacts against concrete blocks. In 4th International Conference on Impact Loading of Structures and Materials (ICILSM)

Presentation at national conference:

- Chambino, M., et al. (2023). Comportamento do betão face a impactos de alta velocidade. Encontro de Ciências Militares 2023.

2. Literature review

2.1 Introduction

The analysis of the phenomenon of the impact of a body against another has been, over time, the target of interest of many researchers. For instance, Johnson and Goldsmith have authored crucial books on this topic [8], [9]. Before World War II, Robins [10], Ponsolet (1830), and Resel (1895) carried out the first studies that focused on simulating aspects such as the depth of penetration of the projectile as a function of its mass, velocity, and the resistance of the semi-infinite environment. However, this approach needed to be revised with the advent of reinforced concrete structures and the need to design them to resist impact loads.

The first contemporary studies about the effect of impact forces on reinforced concrete structures were aimed at military applications. Much of the work during and after the Second World War was aimed at building reinforced concrete structures impenetrable to ballistic weapons and resistant to blast actions [11], [12]. With the development of the nuclear industry, the problem has taken on a different relevance. The research by Chang [13], Hughes [14], and Haldar [15], [16] was pivotal in developing design criteria for nuclear reactors under impact loads. This has led to the correct design of structures capable of withstanding various levels of impact, from plane crashes to pipeline bursts. In this way, the nuclear industry ended up being the great driver of this type of evaluation, sometimes leading to the development of methodologies that would allow a more systematic analysis.

With the emergence of computational tools that allow a less time-consuming numerical analysis, the concern with this topic has extended to other application areas, such as safety barriers [17], maritime structures [18], or even industrial complexes subject to possible accidental impacts [19].

Concrete, as a widely used construction material, has undergone significant evolution in response to the study of its behaviour under high-velocity impacts. Over the years, researchers have investigated various concrete types, including normal strength, high strength, and ultra-high strength concrete, to assess their performance in the face of extreme dynamic loads. Normal strength concrete, characterized by its moderate compressive strength, has been the baseline for many impact studies [20]. High strength concrete, which features enhanced compressive strength, offers improved resistance to impacts and structural integrity [21]. In recent years, ultra-high strength concrete has garnered attention for its extraordinary strength properties, making it a promising candidate for critical infrastructure that requires exceptional impact resistance [22]. These advancements in concrete strength have played an important role in enhancing the resilience of structures subjected to high-velocity impacts, contributing to the safety and security of various applications.

High-velocity impacts involve extremely high-speed collisions between objects, which can lead to significant damage and deformation of the impacted material. One type of high velocity impact is an Explosively Formed Projectile (EFP), among the commonly used Improvised Explosive Devices

(IEDs), devices associated with the most severe impact actions, with high penetration power in vehicles and/or buildings.

2.2 Characterization of the behaviour of concrete against impacts

An impact is characterized as the collision between two bodies, involving the application of force or impetus when one body strikes another. This collision results in the sudden application of a time-dependent load.

The projectile impact on concrete can be classified into two categories: hard and soft impact [23]. The hard impact is characterized only by the deformation of the reinforced concrete element, while the deformation of the projectile is almost non-existent. In soft impact, deformation of the reinforced concrete element and the projectile can be observed. Depending on the nature of the impact in question, the affected element will react structurally in different ways:

- When subjected to a hard impact scenario, the damage is primarily confined to the local region surrounding the impact zone. A substantial amount of the impact energy is dissipated within this area. Conversely, the projectile itself undergoes minimal deformation and remains relatively intact;
- In a scenario involving a soft impact, the structural element experiencing the impact is influenced not only by its own deformation but also by the deformation of the projectile as a whole;
- Under intermediate impact scenarios, the response of the impacted element is contingent upon its inherent resistance. In some cases, the element may exhibit structural behaviour resulting in local and global damage, while in others, only global damage may be observed.

For the local responses of concrete targets hit by projectiles, based on the initial impact velocity of the projectile (v_0), four penetration regimes may be defined, each characterized by distinct approaches regarding the projectile deformation when compared to the deformation of the target [24, 25]:

- Non-deformable regime ($v_0 \leq 0.9$ km/s). Since the projectile is much stiffer than the target, for these impact velocities, the projectile can be considered a rigid body [26]. In this regime, conventional material strength parameters of the target, such as strength, stiffness, hardness, and toughness, govern the extent of the penetration [27];
- Semi-rigid mass abrasive penetration regime (0.9 km/s $< v_0 \leq 1.5$ km/s). The abrasive effect on the projectile during penetration must be considered;
- Semi-hydrodynamic regime (1.5 km/s $< v_0 \leq 3.0$ km/s). This regime applies to armour piercing (AP) typology projectiles. For such impact velocities, the projectile erosion is considerable and must be counted for. Alekseevskii [28] validated Alekseevskii-Tate

model ranges from 1.0 to 3.0 km/s depending on the target and projectile material properties;

- Hydrodynamic regime (v_0 > 3.0 km/s). This regime applies, for example, to space impact debris. The interaction between the colliding objects must consider fluid dynamics interaction [29].

Alternatively, the projectile's penetration into the target may simply be classified into two fundamental processes: sub-hydrodynamic and hydrodynamic. In the sub-hydrodynamic process, the strength of the material plays a crucial role, while in the hydrodynamic process, the material strength has a relatively low impact [30].

2.2.1 Behaviour of concrete under dynamic loading

Understanding the behaviour of concrete under dynamic loading is crucial for designing resilient structures for extreme events, such as earthquakes, explosions or high-speed impacts. By improving our understanding of the behaviour of concrete under dynamic loading, we can develop more effective and efficient materials and structures capable of withstanding extreme events and minimizing the risk of catastrophic failure.

When exposed to dynamic or static loads, concrete displays varying characteristics. Dynamic loading leads to an increase in both the initial stiffness and ultimate strength of concrete when subjected to compression or tension. However, specific dynamic actions such as impacts or explosions exhibit distinct behaviour in terms of the magnitude of the imposed load and duration of the action, which differ from other dynamic actions.

Concrete is generally characterized by its compressive and tensile strengths. The influence of strain rate on concrete material is traditionally quantified using a dynamic increase factor (DIF). This factor represents the ratio of concrete's uniaxial dynamic strength to its equivalent quasi-static strength. It's important to note that distinct DIF values apply to the compressive and tensile strengths of concrete [31]. The analysis suggests that the dynamic increase factor follows a bilinear pattern in a log-log plot, with no noticeable rises for strain rates lower than 10^{-6}. Additionally, the slope exhibits a change at a strain rate of 1 s^{-1} [32].

Several DIF formulas have been introduced in the literature, each utilizing distinct sets or combinations of experimental data. The DIF equations proposed in CEB-FIP [33] are commonly used. Figure 2.1 provides a visual comparison between the CEB compressive DIF formulas and relevant experimental data.

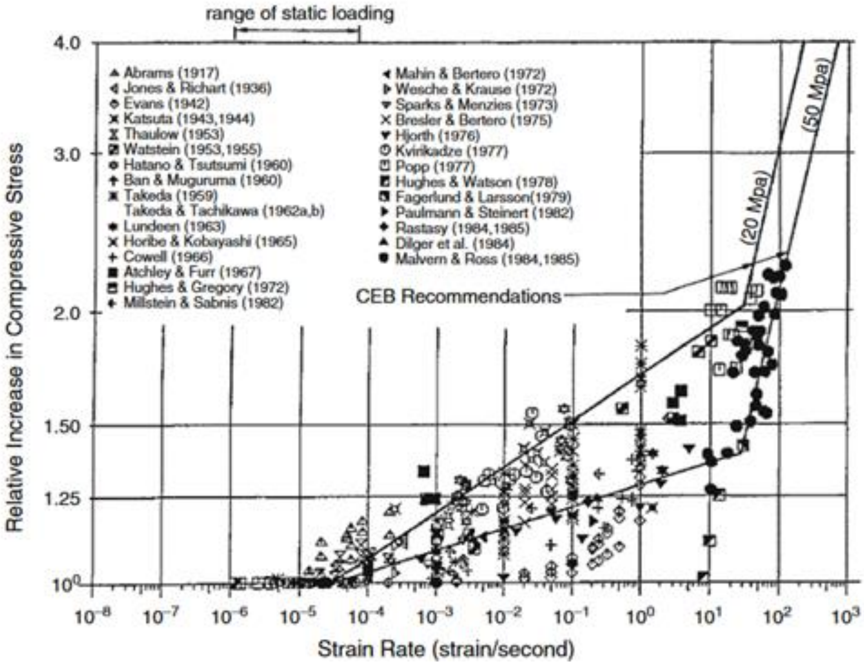

Figure 2.1: Comparison between the CEB compressive DIF formulas and relevant experimental data [33].

Zielinski [34] employed a phenomenological approach in his study, which involved a comparison of static and dynamic tensile loading. He noted a dynamic change in the geometry of the fracture plane. As the loading rate increased, there was a notable increase in aggregate fracture. Additionally, at higher loading rates, multiple fractures were observed, as depicted in Figure 2.2.

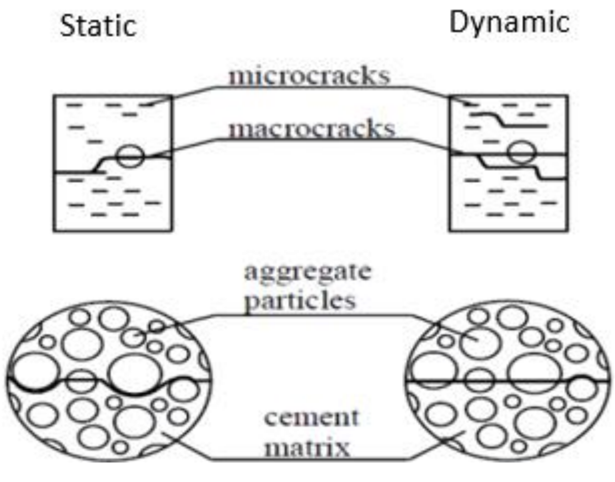

Figure 2.2: Difference of crack pattern for tensile static and dynamic loading [34].

2.3 Failure mechanisms of concrete against impacts

When subjected to impact, concrete is crushed, and cracks and vibrations are induced. When impact occurs on a concrete structural element, the pressure applied by the projectile's tip is much greater than the unidirectional dynamic resistance. Additionally, a shock wave is transmitted from the projectile's tip, reflected on the face opposite to the impact, causing tensile stresses [35]. In Figure 2.3, we can see what happens to concrete when subjected to an impact.

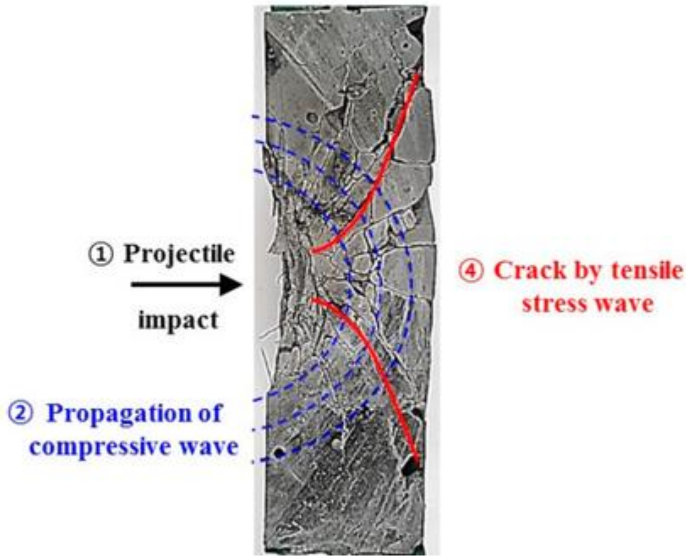

Figure 2.3: Concrete when subjected to an impact [36].

Since concrete has low tensile strength, this phenomenon can lead to scabbing failure and lateral cracking if this strength is exceeded. Both compressive and tensile strengths are essential for evaluating failure mechanisms [37].

The local response of concrete to the impact of a non-deformable projectile is summarized in four successive phases:

As illustrated in Figure 2.4, penetration can be defined as the combined depth of the spall crater plus the tunnelling depth. Where tunnelling is defined as the infiltration or digging of a projectile into the concrete target beyond the depth of the crater. The tunnelling forms a hole inside the target with a slightly greater diameter than the projectile's diameter. Penetration can be explained as when the missile goes through a semi-infinite medium of a target, it causes no effect on the rear face [29, 37].

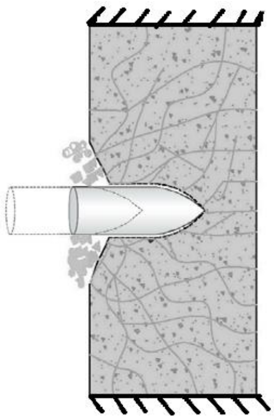

Figure 2.4: Penetration of concrete caused by a projectile [38].

Cone cracking and plugging in concrete represent complex reactions to projectile impacts. This phenomenon occurs during the transition phase between penetration and scabbing. When a missile with plastic characteristics carries more energy than the elastic waves interacting with the rear surface of concrete targets, it initiates the formation of curved shear cracks resembling a bell-shaped plug, a phenomenon referred to as cone cracking and plugging [37]. Figure 2.5 illustrates the occurrence of cone cracking and plugging.

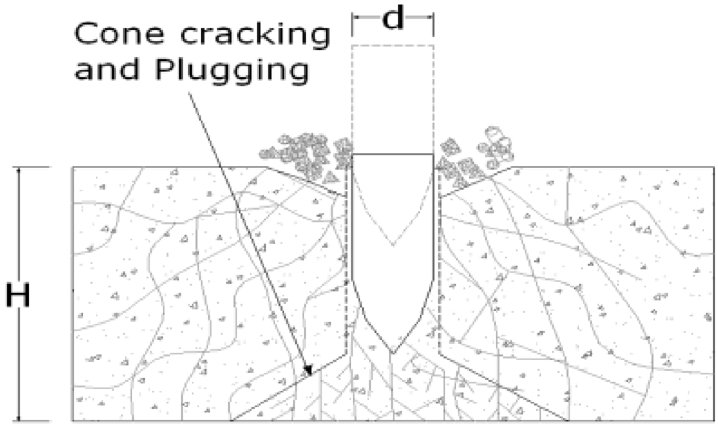

Figure 2.5: Cone cracking and plugging in local impact phenomena caused by a projectile [39].

Spalling occurs when the dynamic force in the shape of waves generated by the projectile within the target becomes equal to or greater than the tensile strength of the target and forces the bell plug and shears-off the surrounding material of the target from the back face of the target. Generally, the zone of spalling is wider than the zone of scabbing however, the zone of scabbing has greater depth than the spalling. Once the scabbing is observable on the target, no further strength remains in the concrete target to resist further local impact effects [29, 37]. Experiments have shown that spalling is reduced by increasing the reinforcement, since the reinforcement will hold the concrete fragments (confinement effect) [40]. In Figure 2.6, we can observe scabbing and spalling caused by a projectile.

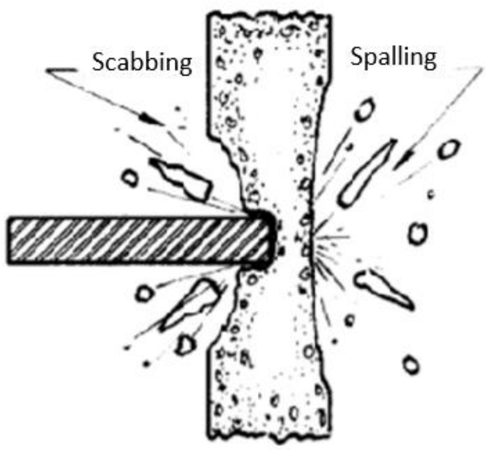

Figure 2.6: Scabbing and spalling caused by a projectile [28].

Perforation is the last process of damage due to hard missile impact. Perforation means complete passage or complete crossing of the projectile through the target. It causes the missile to extend the penetration hole through the scabbing crater and exit from the rear face of the target [29, 37], as represented in Figure 2.7.

Figure 2.7: Perforation of concrete caused by a projectile [28].

2.4 Equation for projectile penetration of concrete

This subsection reviews the available formulas to estimate the penetration of projectiles into concrete. The discourse begins by addressing the earliest formulations and traces the evolutionary path that has led to the latest equations in use today.

2.4.1 Modified Petri formula

Petry's research in 1910 resulted in the formulation of a predictive equation that estimated the depth of penetration of a Hard-type impact projectile into a semi-infinite concrete element. The formula is expressed as follows:

$$x = 12k_p A_p \log_{10}\left(1 + \frac{v_0^2}{215{,}0}\right) \tag{2.1}$$

where,

x: penetration depth, in inches;

k_p: penetration factor for reinforced concrete;

A_p: missile's weight relative to the area (lb/ft^2);

v_0: striking velocity in ft/sec.

Initially, the k_p values were 0.00799 for massive concrete, 0.00426 for regular reinforced concrete, and 0.00284 for specially reinforced concrete. Note that these k_p values are independent of concrete strength and only depend on how the concrete is reinforced. [41] Amerikan subsequently revised the k_p values to consider the strength of concrete, particularly reinforced concrete. The revised k_p values are sometimes used for regular reinforced concrete. The revised k_p values as a function of concrete strength are shown in Figure 2.8. The graph of revised k_p values can be seen in reference [41].

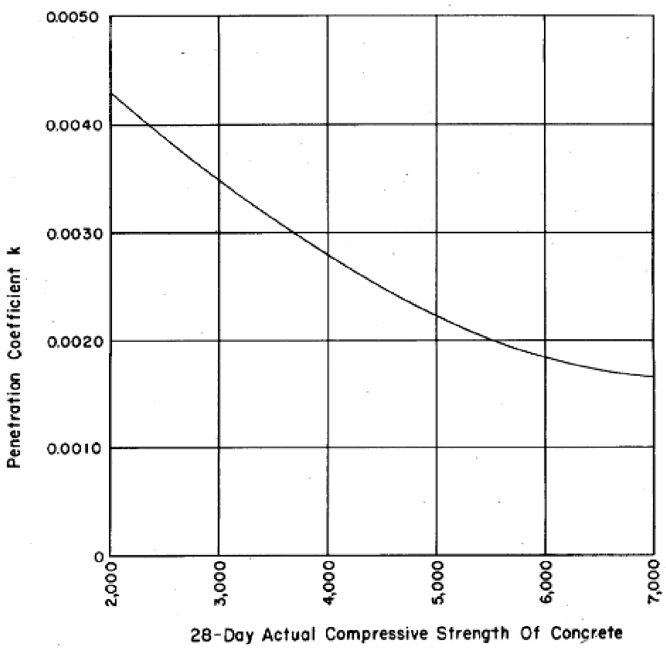

Figure 2.8: Graph of revised kp values [41].

2.4.2 Modified NDRC Formula

In 1946, the National Defense Research Committee introduced a formula for a non-deforming projectile designed to penetrate a solid concrete target. The empirical formula's development was based on readily available experimental data collected from various tests. The NDRC equation is presented in equation 1.2.

$$G_{(x/d)} = KN^{*}d^{0,2}\left(\frac{w}{d^3}\right)\left(\frac{v_0}{1000}\right)^{1,80} \tag{2.2}$$

where,

$G_{(x/d)} = \left(\frac{x}{2d}\right)^2, for \frac{x}{d} \leq 2.0$

$G_{(x/d)} = \left(\frac{x}{d}\right) - 1, for \frac{x}{d} \geq 2.0$

d: diameter of the projectile in inches;

w: weight of the projectile in pounds;

v_0: striking velocity in ft/sec;

x: penetration depth, in inches;

N^{*}: missile shape factor defined in equation 1.3.

$$N^* = 0.72 + 0.25\sqrt{n - 0,25} \quad (2.3)$$

The concrete penetrability factor, K, was not made publicly accessible until Kennedy defined K in terms of the concrete's compressive strength, f_c' in psi, as defined in equation 1.4 [41].

$$K = \frac{180}{\sqrt{f_C'}} \quad (2.4)$$

The Modified NDRC Formula is obtained by merging the original NDRC formula outlined in Equation 1.2 with Equation 1.4, thereby producing a new expression considering the concrete penetrability factor, K.

2.4.3 Whiffen formula

The Whiffen formula has expanded the applicability of the prediction equations to larger projectile diameters by using concrete penetration data for larger projectiles, fragment and bomb penetration striking reinforced concrete. The Whiffen Formula also takes into account a factor that depends on the size of the concrete aggregate [42]. The limitations of the formula shown in equation 1.5 are as follows:

800 < f'_c concrete compressive strength) < 10,000 psi;

0.3 < M (mass of the projectile) < 22,000lb;

0.5 < d (diameter of the projectile) < 38 inches;

0 < V_0 (projectile striking velocity) < 1750 ft/s;

0.5 < d/a (a represents the maximum aggregate size in inches) < 3.5.

$$\frac{x}{d} = \left(\frac{870}{\sqrt{f_C'}}\right)\left(\frac{M}{d^3}\right)\left(\frac{d}{a}\right)^{0,1}\left(\frac{v_0}{1750}\right)^n \text{ where } n = \frac{10,70}{\sqrt{f_C'}} \quad (2.5)$$

2.4.4 Kar formula

The Kar formula, quite similar to the modified NDRC formula, considers the type of material of the missile in terms of Young's modulus. Using the NDRC and Kar formulas to predict the penetration depth of a steel missile would yield identical results [42]. The Kar Formula is represented by equation 1.6.

$$G_{(x/d)} = \frac{180N^*M}{d\sqrt{f_C'}}\left(\frac{E}{E_s}\right)^{1,25}\left(\frac{v_0}{1000d}\right)^{1,8} \quad (2.6)$$

where,

E_s: Young's modulus of steel in psi or ksi;

E: Young's modulus of the missile material in the same units as E_s;

N^*: missile shape factor defined in equation 1.3;

M: projectile weight in pounds;

d: diameter of the projectile in inches;

f_C': concrete compressive strength in psi;

v_0: projectile striking velocity in ft/s.

The G-factor calculated from equation 1.6 would then be used in equation 1.2 to obtain the predicted penetration depth.

2.4.5 Amman and Whitney formula

The Amman and Whitney Formula can be employed to estimate the penetration of explosively achieved small fragments traveling at velocities greater than 305 m/s [42].

$$\frac{x}{d} = \frac{282}{\sqrt{f_C'}} N^* \left(\frac{M}{d^3}\right) d^{0,2} \left(\frac{v_0}{1000}\right)^{1,8} \tag{2.7}$$

where,

x: penetration depth, in inches;

d: diameter of the projectile in inches;

f_C': concrete compressive strength in psi;

N^*: missile shape factor defined in equation 1.3;

M: projectile weight in pounds;

v_0: projectile striking velocity in ft/s..

2.4.6 Sandia penetration equations

In 1997, Sandia National Laboratories published penetration equations for various materials; concrete is one of those materials. Equation 1.8 provides the penetration for a projectile moving with a velocity greater than 200 ft/s and striking a soil, rock, or concrete target.

$$D = [0.00178SN \left(\frac{w}{A}\right)^{0.7} (V - 100)]K_h \tag{2.8}$$

where,

D: penetration distance in feet;

w: weight of the projectile in pounds;

A: cross-sectional area of the penetrator;

K_h: scaling factor for projectile weights under 400 pounds

The definitions of the terms S (for concrete), N, and Kh used in the previous equation can be found in equations 1.9, 1.10, and 1.11, presented below.

$$S = 0.085K_e(11 - P)(t_cT_C)^{-0.06}\left(\frac{5000}{f_C'}\right)^{0.3} \tag{2.9}$$

$$N = 0.18\,(CRH - 0.25)^{0,5} + 0.56 \tag{2.10}$$

$$K_h = 0.4w^{0,15}\ when\ W \leq 400\ lbs \tag{2.11}$$

In equation 1.9, P is the volumetric percent rebar, t_c is the cure time in years and must be ≤ 1, T_C represents the thickness of the target in terms of penetrator diameters, with an upper limit of 6, and K_e for unreinforced concrete equals $(30/W)^{0.3}$.

Provided that the equations are applied within their explicitly defined constraints, the outcome can be expected to be reasonably precise, with an error margin of around 15%. Nonetheless, it should be noted that the accuracy of the result may be compromised when the limits of applicability are approached or exceeded. The Sandia penetration equations have specific limitations that determine when they are applicable: [43].

-The penetrator remains undamaged throughout the penetration process;

-The penetrator maintains a relatively stable trajectory;

-The impact velocity is under 4000ft/s;

-If the penetration depth is less than three calibres, the equations' reliability may questionable;

-These equations are exclusive to the materials explicitly mentioned;

-For concrete targets, a minimum penetrator weight of around 10 pounds is required.

2.4.7 Unified facilities criteria formula

The UFC, specifically UFC 3-340-02, is a comprehensive compilation of information and guidelines dedicated to designing structures that can effectively withstand the effects of accidental blasts. Nonetheless, the document contains a section solely dedicated to the estimation of fragment penetration in concrete. This estimation considers a range of factors, including projectile diameter, weight, striking velocity, calibre density, nose shape, and the unconfined compressive strength of the concrete, among others [44]. By incorporating all of these critical variables, the UFC provides a reliable and comprehensive framework for designing structures that can withstand the potentially catastrophic impacts of accidental blasts. For concrete penetration by armour-piercing fragments, the estimated depth can be estimated using equation 1.12 in combination with equation 1.13.

$$\begin{cases} X_f = (4.0E^{-3})(KN^*D)^{0,5}d^{1,1}V_s^{0.9}\ for\ X_f \leq 2d \\ X_f = (4.0E^{-6})KN^*Dd^{1,2}V_s^{1.8} + d\ for\ X_f > 2d \end{cases} \tag{2.12}$$

$$K = \frac{12,91}{\sqrt{f_C'}} \tag{2.13}$$

where,

X_f: penetration by armor-piercing steel fragments in inches;

K: penetrability constant;

N^*: missile shape factor defined in equation 1.3;

D: Caliber density, or W/d^3 in lb/in^3 ;

d: Fragment diameter in inches;

V_s: Striking Velocity (ft/s);

f_C': concrete compressive strength in lb/in^2.

In cases where concrete is penetrated by fragments that are not armour-piercing, the penetration depth can be adapted by employing a constant that accounts for the properties of the fragment material. The estimated penetration of a non-armour piercing fragment can be calculated using equation 1.14.

$$xX_f' = kX_f \tag{2.14}$$

where,

X_f': maximum penetration of a non-armor piercing fragment;

k: constant dependent upon the casing metal;

X_f: penetration calculated by Equation 1.12;

The given values of k, from Table 4-16 of Reference [42] are shown below;

-Armor-piercing steel, k = 1.0;

-Mild steel, k = 0.7;

-Lead, k = 0.5;

-Aluminum, k = 0.15.

2.5 High-velocity impacts

Explosive materials can damage a structure through two distinct mechanisms: the resulting blast wave exerts pressure, and high-speed fragments are launched to impact the surface.

Detonations occur rapidly, within a few microseconds, and release a substantial amount of energy. The gases produced by the detonation are highly compressed, creating shock waves that propagate through the air [45].

Explosive materials find their applications in a diverse range of military and industrial industries. These include explosive welding, shaping, and compacting of powders, rock fragmentation, and the formation of projectiles or jets through shaped charges or EFP’s. In demolition applications, these explosives may be employed directly or as the filling for shaped charges or EFP’s, which generate high-velocity projectiles used to cut or demolish structures [46].

Typically, a shaped charge refers to a cylindrical explosive charge with a cavity, either lined or unlined, at one end. The detonation process of a typically shaped charge involves initiating a detonator-booster explosive train, which then detonates a circular cylinder of explosive. The detonation of the cylinder leads to the collapse of a metallic-lined conical cavity located at the opposite end of the detonator, resulting in the formation of a jet [47]. Figure 2.9 shows a shaped charge with a booster at the rear and a liner at the front.

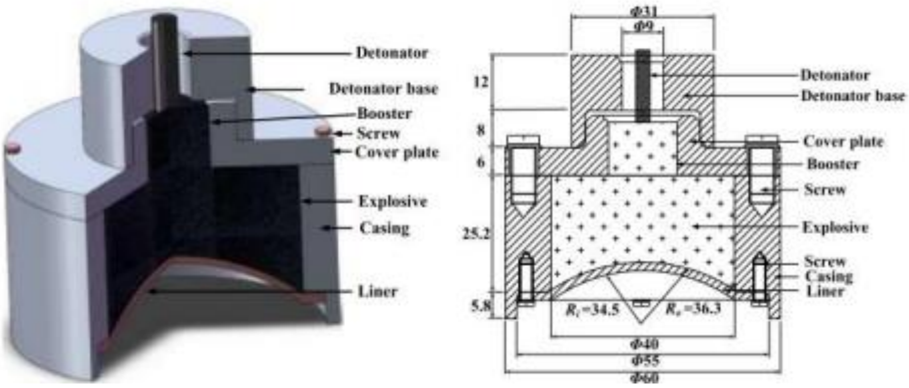

Figure 2.9: Constitution of a shaped charge [48].

After the explosive detonates, a shock wave propagates outwards, deforming the metal disk and forming a projectile, which travels at high speed. The projectile elongates during its displacement until it reaches the target's surface, initiating the phenomenon of penetration. The projectile's velocity gradually decreases as penetration increases, and fragmentation of the projectile may occur during impact until finally, the maximum penetration depth is reached [49].

The Explosively Formed Penetrator/Projectile exhibits similar behaviour to shaped charges. It is typically made up of a metal plate or cone that is explosively formed into a streamlined shape when detonated. The device is placed in a container or casing, then aimed at the target which can be placed at a greater distance than the shaped charge. The explosive’s detonation generates a shock wave that propagates outwards, deforming the metal disc and forming a projectile that travels at high-speed (Misznay Shardin effect) [50] while the shaped charge uses the Munroe effect [46]. Figure 2.10 shows the constitution and formation of an EFP.

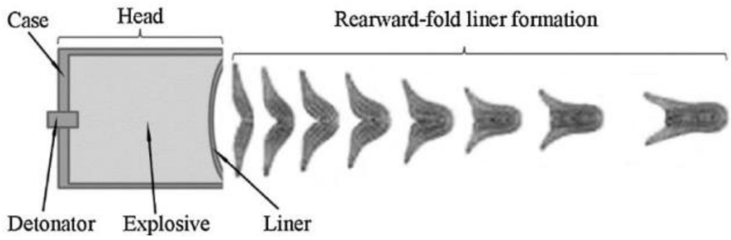

Figure 2.10: Constitution and formation of Explosively Formed Penetrator [46].

EFPs are a particularly dangerous type of IED because they can penetrate armour plating and other protective barriers that generally offer some degree of protection against other types of explosive devices. They have been used extensively by insurgent and terrorist groups in various conflicts around the world, including Iraq and Afghanistan [47].

Fang also mentions that studies are few regarding the penetration of these projectiles into reinforced concrete structures, and the impact phenomenon is far from being understood by the scientific community [47]. Figure 2.11 shows reinforced concrete after an EFP impact.

Figure 2.11: Reinforced concrete after EFP impact [52].

2.5.1 The Gurney velocity approximation

The Gurney model provides straightforward algebraic relationships for predicting the velocity transferred to a metal when it comes into contact with a detonating explosive. This makes the Gurney method a versatile tool applicable to various scenarios involving explosive-metal interactions. It facilitates the execution of design and parametric analyses with ease. The Gurney model finds utility in a range of applications, including the design of warheads and fragmentation devices, assessing the efficiency of converting chemical energy from high explosives into the kinetic energy of a plate, initiating explosives through the impact of an explosively driven plate, launching dielectric plates using electrical detonation of a metal foil, and determining the velocities of metal fragment layers in the context of shock wave physics [53].

This basic and rough analysis operates under the assumption that the potential (or chemical) energy stored in the explosive charge before detonation is entirely transformed into two forms: the kinetic energy of the metal after detonation and the expansion of the explosive byproducts. Consequently, it presumes that a specific energy value (energy per unit mass) associated with a particular explosive is transitioned from its chemical energy state at the outset to kinetic energy in the concluding state [54].

This energy is referred to as the Gurney energy, denoted as 'E,' and represents a portion of the overall chemical energy released during detonation. The ultimate kinetic energy is distributed between the propelled metal and the gases produced during detonation, based on a presumed linear velocity profile within the gases. It is further assumed that the expansion of the detonation products occurs uniformly and maintains a constant density [55].

M, Weld [55] presents a comprehensive mathematical derivation leading to the final equation for the open-faced sandwich structure as depicted in equation 1.15.

$$V = \sqrt{2E}\left[\frac{\left(\left(1+\frac{2M}{C}\right)^{8}\right)+1}{6\left(1+\frac{M}{C}\right)}+\left(\frac{M}{C}\right)\right]^{-1/2} \tag{2.15}$$

where,

V: projectile velocity;

M: initial mass of the flyer;

C: charge weight;

E: specific explosive kinetic energy of the explosive used.

2.6 Numerical analysis of impacts

This subsection introduces a selection of the most important studies, according to the author, that laid the foundation for the subsequent chapter's investigation. These studies not only formed the groundwork for constructing the EFP model but also provided essential guidance for developing the subsequent model concerning to the impact of projectiles on concrete.

To simulate the entire process of formation, flight, and penetration of an explosively formed projectile (EFP), WU used a 3D coupled hydrocode of LS-DYNA. The EFP was an overturned shaped charge with a calibre of 60 mm, and the fluid-solid coupling problem was addressed using the Arbitrary Lagrangian-Eulerian (ALE) method. A velocity attenuation equation was fitted to predict the flight distance of the EFP. The penetration capability of the EFP against an armour plate was studied using similarity theory and numerical simulation. To validate the equation, a test was carried out to check the speed after perforating a 25 mm steel plate at a distance of 48 meters. By comparing the simulation and experiment, crucial solutions were obtained, including the optimized charge structure of the EFP, ideal projectile shape, flight process attenuation rule, and penetration capability after 48 meters of flight. The numerical solution was consistent with the experimental data, and the findings provide vital guidance for the engineering design of EFP's. Figure 2.12 represents the projectile's formation over time and the air movement around it during flight based on the simulation [56].

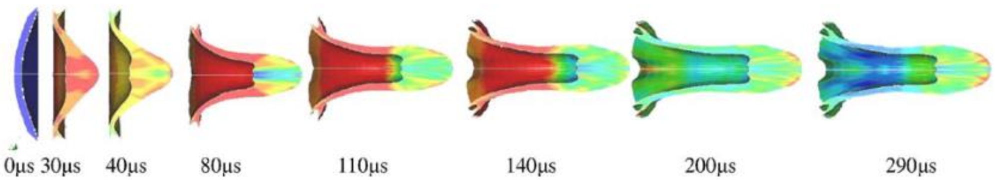

Figure 2.12: The formation process of 60 mm charge calibre EFP in the air [56].

Figure 2.13 shows a comparison between the projectile obtained through numerical modelling and the projectile obtained through an experimental campaign.

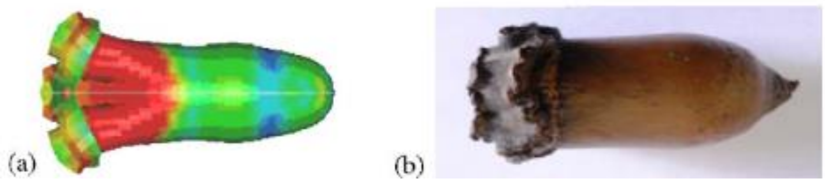

Figure 2.13: The shape comparison between the simulation (a) and the experimental projectile (b) [56].

Figure 2.14 illustrates a comparison between the actual and simulated impact processes, leading to the conclusion that the processes were very similar.

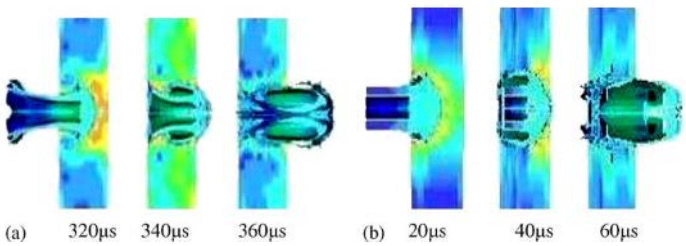

Figure 2.14: Comparison of the penetration process between (a) EFP and (b) simulated EFP [56].

According to the conducted analysis, the authors concluded that an ideal shaped charge can be achieved by utilizing the EFP charge structure and a cover shape that combines an arc and a cone. This type of charge exhibits a high velocity and an optimal length-to-diameter ratio. The simulation and theoretical outcomes aligned with the experimental results, indicating that the simulation can accurately predict the projectile's shape, mass, velocity, flight stability, and penetration ability. The ALE technique was effective in simulating the fluid-solid coupling problem [56].

Alternatively, Zakir and colleagues [57] aimed to investigate the influence of liner's thickness, explosive type, and length-to-diameter ratio of charge (L/D) on the formation and effectiveness of EFP, measured in terms of penetration in Rolled Homogeneous Armor (RHA) targets. The study employed explicit finite element (FE) hydrocode ANSYS/Autodyn to perform simulations. The explosive was modelled using Euler processor, while the liner and casing were digitally divided into discrete elements using the Lagrange processor. The interaction between explosive gases and the casing/liner was achieved through the Euler-Lagrange coupling technique. The study showed that reducing the liner thickness from 6 to 4 mm enhances the velocity of the high-speed projectile formed without compromising the structural integrity of the EFP [57].

Furthermore, the use of charge types with higher velocities of detonation (VOD) increased the velocity of the high-speed projectile. The study also revealed that HMX-based charges significantly increase projectile velocity and penetration in RHA targets. Increasing the length-diameter ratio of the system from 0.75-1.1 can lead to the formation of either a high-speed projectile or a long stretchy projectile. Field tests were conducted to validate the numerical results. The simulations demonstrated that decreasing the thickness of the liner can increase EFP velocity by 40% and penetration depth in RHA by 31%. Moreover, using HMX-based charges for a length-to-charge diameter ratio of 1.0 results in a 21% increase in EFP velocity and a 35% increase in penetration depth in RHA. This research provided EFP designers with optimal high-speed projectile options by incorporating different geometrical parameters [57].

During field tests and experiments, the developed copper EFP successfully penetrated through steel targets upon initiation. In addition, penetration simulations were conducted for a few selected EFP configurations against steel targets, whose results are depicted in Figure 2.15. The simulation outcomes closely agree with the experimental ones, thereby validating the simulation model. The copper EFP also exhibits enough residual velocity and mass to penetrate the steel target.

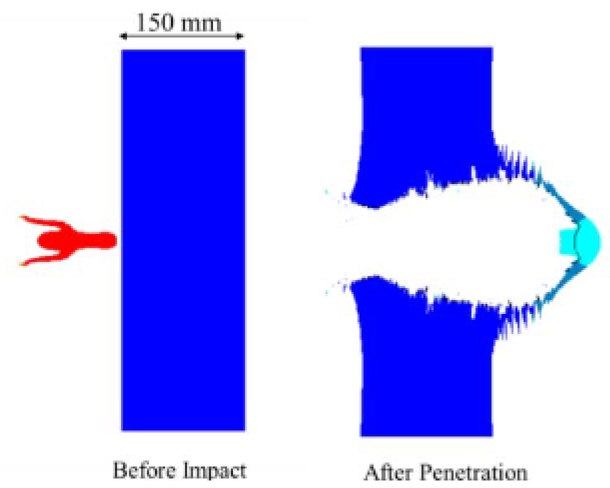

Figure 2.15:The penetration simulation results in Steel Target [57].

Figure 2.16 displays the developed EFPs from three distinct charge types, indicating that the profiles and velocities of the resulting high-velocity projectiles differ. The charge type LX-14 attains the highest velocity and penetration performance in RHA among the developed EFPs, followed by HMX-9010 and Comp-B. This is attributed to the higher detonation velocity and C-J pressure of HMX-based charge types, which generate more elongated and high-speed projectiles than RDX-based charge types like Comp-B.

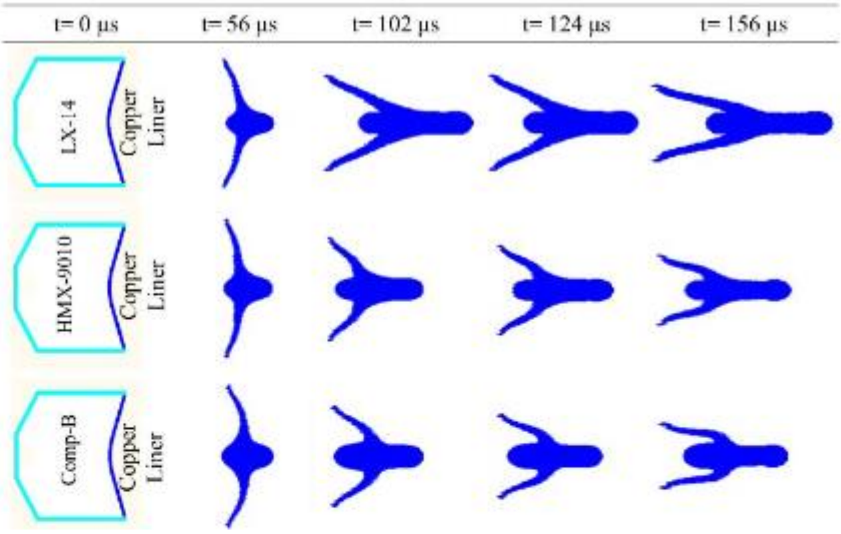

Figure 2.16: EFP formation process from three different types of charge [57].

A numerical simulation methodology for replicating explosively formed projectiles' formation and ballistic capabilities was introduced by Cardoso and team [58]. The study assessed various EFP configurations, materials, and detonation conditions based on their resulting projectile performance, including stable flight velocity. The proposed model features a generic EFP with an aspect ratio of around 1 and a 5 mm case/base thickness. Specific contact algorithms establish dynamic interactions between the components of the EFP, allowing for the interpolation of pressure from detonation to other components, resulting in deformation and acceleration of the EFP. The model undergoes validation against experimental observations and is then utilized to evaluate the impact of liner materials and thickness, high-explosives, number, and off-centre distance of detonators. EFP performance was quantified using non-dimensional geometrical parameters derived from their configuration. The study revealed that liner thickness (and variability), and off-centre distance of detonators are crucial factors for EFP performance. Among the materials and parameters tested, the highest performing EFP features a copper liner, dynamite high-explosive, and a liner thickness between 4 and 7% of its diameter [58].

The analysis of the developed models was conducted in two distinct stages. During the first stage, which spans around 10 μs of the process, the explosive detonation, shock wave propagation, and resulting interaction of detonation products cause the liner to deform and accelerate. During the second stage, which spans approximately 400 μs, the direct effects of the explosive, casing, and base are disregarded. The focus is solely on modelling the stabilization of the projectile's speed and deformation [58].

During the formation of the EFP, velocities are observed to reach a maximum in the initial stages ($0 < t < 100$ μs) due to the interaction of the detonation wave with the liner. Subsequently, during the stages between 100 and 400 μs, the liner deforms to form the projectile, and the speed stabilizes. Stable flight speed is achieved around 400 μs. Copper was found to have the optimal capacity to form an EFP with high penetration capability due to its density and ductility. Dynamite had the most significant effect on the final configuration of the projectile due to its speed of explosion and energetic capability. Overall, copper and dynamite were found to be the most efficient combination in terms of final kinetic energy [58]. Figures 2.17 display the development of EFP velocity throughout its formation process for various liner materials and high explosives respectively.

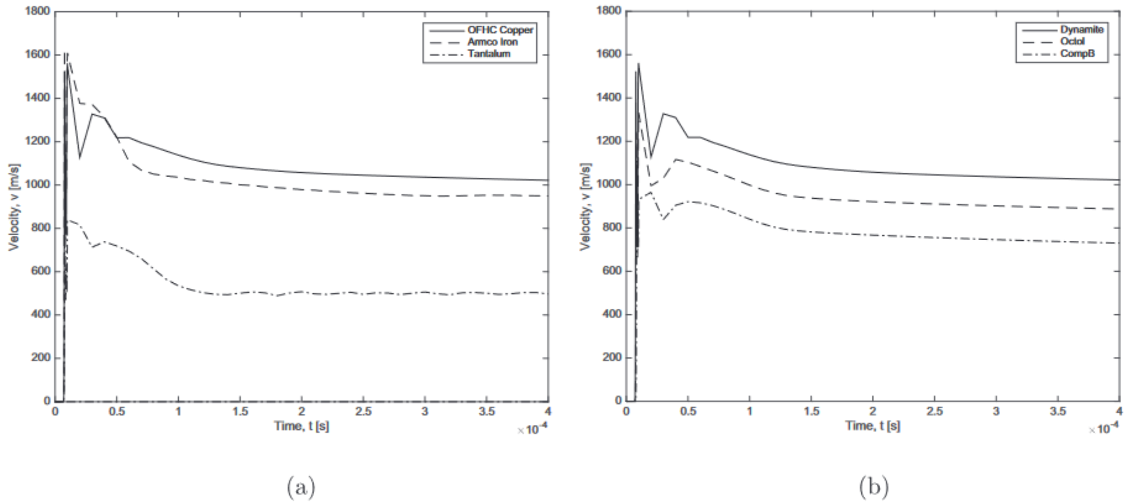

Figure 2.17: Evolution of the projectile velocity for (a) different liner materials (dynamite HE) and (b) different high explosives (copper liner) [58].

Meanwhile, Figure 2.18 illustrates the evolution of the projectile's shape during the initial stages of formation for a 4mm copper liner and dynamite HE.

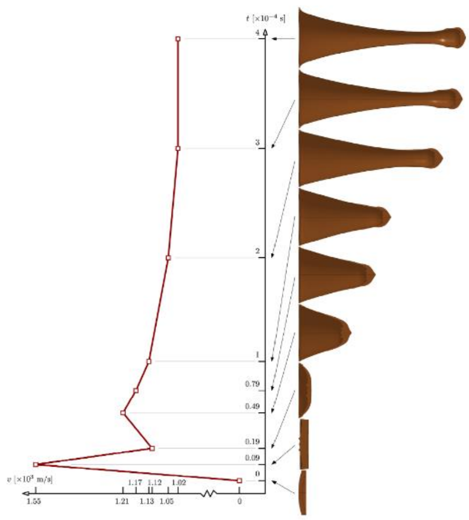

Figure 2.18: Evolution of the shape of the projectile during the early formation stages. [58].

The most recent study in this field, conducted by Li Hao in 2022 [59], investigated the impact of an explosively formed projectile on a large reinforced concrete wall. The research aimed to comprehend how EFP’s can effectively breach reinforced concrete walls. It analysed the combined effects of EFP penetration and explosion shock waves on the concrete wall. Figure 2.19 displays both the experimental setup and the configuration replicated in the numerical model.

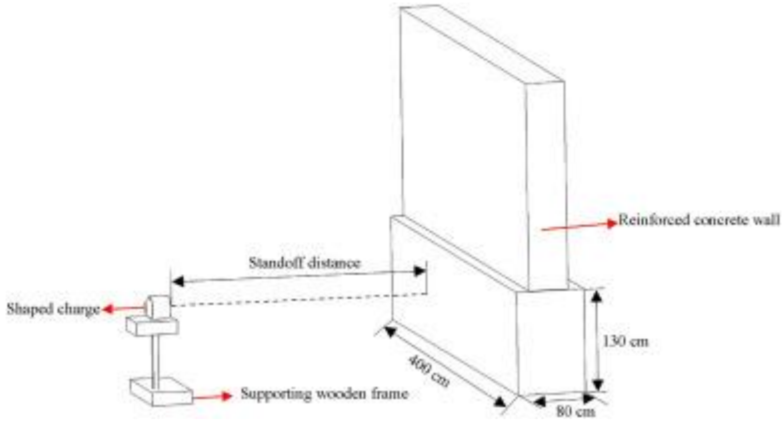

Figure 2.19: Experimental setup used [59].

The findings revealed that the designed shaped charge could create a large, deep crater in the concrete wall. The average crater diameter exceeded 67 cm, which is 5.58 times the charge diameter, with a depth of over 22 cm, corresponding to 1.83 times the charge diameter. EFP penetration primarily caused the wall's failure, resulting in an average crater diameter and depth of 54.0 cm and 23.7 cm, respectively [59].

The explosion shock wave had a minor impact on crater depth, leading to a slight increase, with an average crater depth of 24.5 cm when considering the shock wave [59]. However, it significantly increased the crater diameter, expanding the damage zone. This effect diminished with increasing standoff distance.

Comparing plain concrete walls to reinforced concrete walls, the latter exhibited a 5.94% reduction in crater diameter and a 9.96% reduction in crater depth. When the EFP encountered steel bars, the crater diameter decreased by 1.36% (one steel bar) and 5.45% (intersection of two steel bars), and the crater depth decreased by 4.92% (one steel bar) and 14.02% (intersection of two steel bars). Steel bars caused the EFP to deviate from its trajectory during penetration [59].

A quarter-symmetric 3D numerical model was created to analyse the impact of steel bars. The model considered both the concrete and steel components of the reinforced concrete wall, set within an 80 cm radius air domain to account for combined damage from EFP penetration and explosion shock waves.

The study emphasized the importance of accurate material models, calibration parameters, a 3D model, and simulation algorithms. Mesh refinement was implemented along the penetration path, and fluid-solid coupling was used to model interactions. Non-reflective boundaries and an infinite air domain were incorporated in the model [59]. The final model is depicted in Figure 2.20.

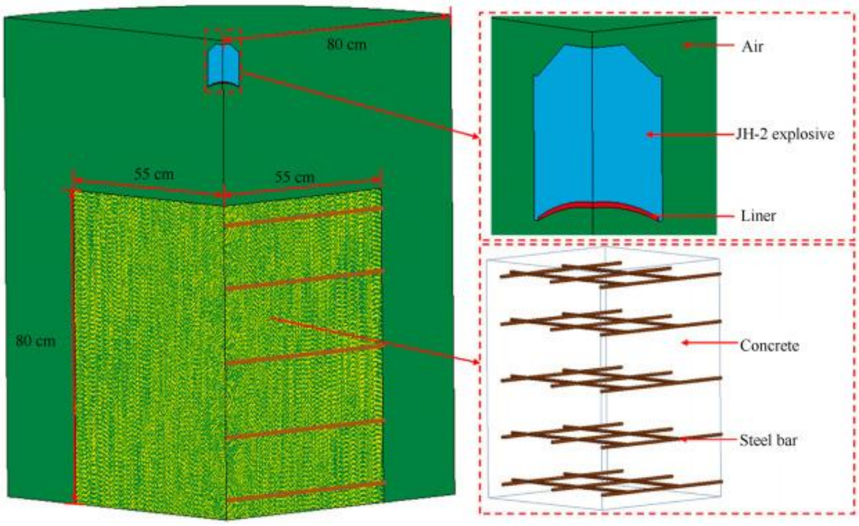

Figure 2.20: Final model [59].

Figure 2.21 illustrates the similarity between the results obtained in the experimental campaign and those from the numerical model.

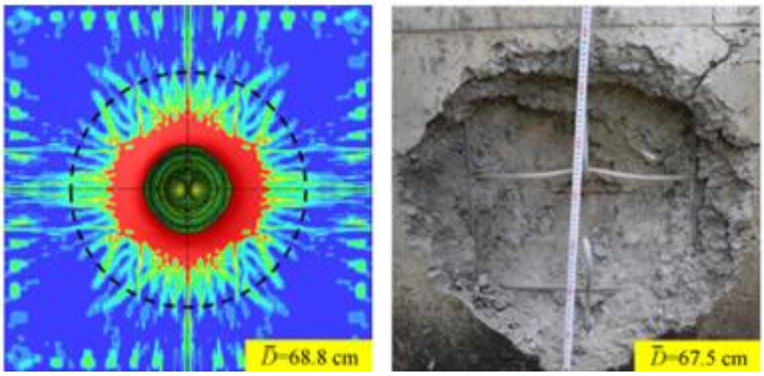

Figure 2.21: Comparison of the numeric model with experimental campaign [59].

3. Numerical design of the EFP

In this chapter, we have made a numerical model of an EFP to evaluate its capacity to achieve the target velocity in the forthcoming experimental campaign. The purpose of this simulation is to confirm the projectile's performance in achieving the desired velocity. In order to achieve this, the LS-DYNA program was used.

LS-DYNA is a finite element analysis software developed by Livermore Software Technology Corporation (LSTC) that is widely used in various engineering fields. It is specifically designed to handle non-linear analysis problems and is known for its accuracy and precision [60,61,62].

The simulation consists of three stages: defining the geometry and mesh, selecting the materials, and specifying the boundary conditions. These stages are performed using LS-Prepost. Once the model is created, calculations are conducted using the LS-DYNA Program Manager. The results are then visualized in LS-Prepost.

3.1 Consistency units

Like other FEM calculation software, LS-DYNA requires the use of a consistent set of units for accurate calculations. The units of physical quantities can be determined based on their characteristics and the equations of mechanics. Equations 3.1, 3.2, and 3.3 provide examples of this.

$$\text{1 unit of force} = \text{1 unit of mass x 1 unit of acceleration} \quad (3.1)$$

$$\text{1 unit of acceleration} = \text{1unit of length} / (\text{1 unit of time})^2 \quad (3.2)$$

$$\text{1 unit of density} = \text{1unit of mass} / (\text{1 unit of length})^3 \quad (3.3)$$

For the numerical model in this thesis, the units used are listed in table 3.1.

Tabel 3.1: Units used in the numerical model.

Length [L]	**Time** [T]	**Mass** **[**M]	**Force** **[**MLT^{-2}]	**Pressure** [$ML^{-1}T^{-2}$]	**Energy** [ML^2T^{-2}]	**Speed** **[**LT^{-1}]	**Density** [ML^{-3}]
mm	ms	kg	kN	GPa	kN-mm	mm/ms	kg/mm^3

3.2 EFP numerical model

3.2.1 Geometry and boundary conditions

Precise replication of geometric configurations and boundary conditions is essential for creating accurate FE models. Figure 3.1 illustrates the geometric configuration of the simulated EFP. This particular geometry was selected following the insights provided by [46], offering a visual representation of its shape and structure.

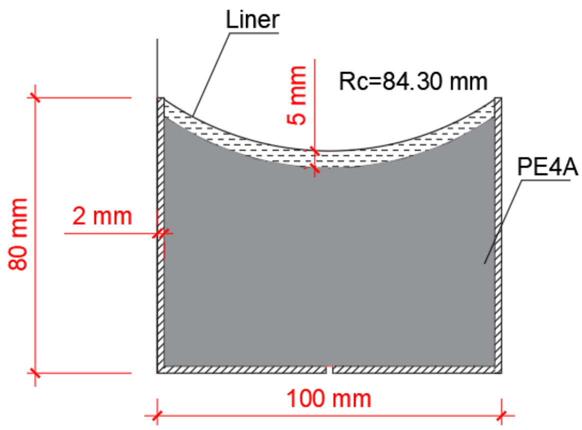

Figure 3.1: Geometrical configuration of an EFP.

Figure 3.2 illustrates a schematic of the bi-dimensional numerical model employed, which was designed as a 2D axisymmetric model. This choice significantly reduces computational costs, ensuring efficient simulations.

Figure 3.2: Schematic view of the numerical model.

A parametric investigation was conducted to evaluate the impact of using a metal casing with identical dimensions. The study revealed that employing a metal casing would enhance the speed by approximately 15%. However, for safety considerations and to prevent potential fragments damage to the surroundings, the PETG casing was retained. The selection of PETG material was also driven by the lack of prior research utilizing 3D printing for EFP production.

The computational models contained two parts: EFP and the air. The fluid–solid coupling computing method is considered in FE models. For the meshing algorithm, a fine mesh size produces more accurate results but requires longer time consumption in comparison with coarse meshing simulations. In the present study, uniform square mesh sizes of 1mm were selected based on the results of mesh sensitivity studies, which were carried out by Agu [63] and Elshenawy [64]. The high explosive was initiated at the centre point of the back of the EFP, and the one-point initiation method was adopted.

3.2.2 Material modelling

Given the challenging conditions of high pressure, temperature, and deformation rates inherent in the formation of the EFP's casing and liner, the selection of an appropriate material model is crucial. The Johnson-Cook constitutive model has been deemed the most suitable approach to accurately predict the material's behaviour under high strain rates [65,66].

This constitutive model is widely recognized and referenced in the field of impact and high strain rate analysis, particularly when considering triaxial stress states that are influenced by both deformation rate and temperature. Additionally, due to the presence of shock waves and elevated pressures within the metallic materials, an equation of state (EOS) needs to be defined in combination with the Johnson-Cook model. The Johnson-Cook effective stress is determined by considering the plastic strain, plastic strain rate, and temperature as variables, as demonstrated in equation 3.4.

$$\bar{\sigma} = (A + B\varepsilon^n)[1 + C\ln(\varepsilon^*)][1 - (T^*)^m] \tag{3.4}$$

In Equation 3.4, the variables A, B, C, and n represent the yield stress, the hardening constant, the strain-rate constant, the hardening exponent, and the thermal softening coefficient, respectively. The effective plastic strain is $\varepsilon^* = \varepsilon \,/\, \varepsilon_0$ and the non-dimensional temperature is $T^* = (T - T_0)/(T_m - T_0)$ where T_m is the melting temperature of the material, T_0 is the room temperature an T is the current temperature.

The Gruneisen equation of state (EOS) is employed alongside the Johnson-Cook constitutive model. This EOS governs the material's response to shock waves and relies on Hugoniot's linear relation between the shock wave velocity (v_s) and the material particle velocity (v_p), expressed as $v_s = c_0 + s v_p$, where c_0 represents the wave speed, and s is a material-specific parameter. In the context of dense materials, the Gruneisen EOS, which establishes the relationship between pressure (p) and internal energy as follows:

$$p = p_0 C_0^2 \mu\psi + (\gamma_0 + a\mu)E \tag{3.5}$$

With

$$\psi = \frac{2 + a\mu^2 + (2 - \gamma_0)\mu}{2\left[1 - (S_1 - 1)u - S_2 \frac{u^2}{1 + \mu} - S_3 \frac{\mu^3}{(1 + \mu)^2}\right]} \tag{3.6}$$

In the equation, γ_0 signifies the Gruneisen coefficient, which represents a first-order energy correction factor, and S_i (where i = 1, . . ., 3) denotes material-specific parameters. Additionally, $\mu = \rho/\rho_0 - 1$ serves as a dimensionless coefficient, calculated in relation to the initial and current material densities [67]. Table 3.2 shows the material property input data and EOS input data [56].

Tabel 3.2: Material property and EOS input data of copper.

Copper										
MAT _JOHNSON_COOK	RO [kg/m³]	G(Gpa)	A(Mpa)	B(Mpa)	N	C	m	Tm	σ	C
	8,97	46,5	90	292	0,31	0,025	1,09	1356	0,09	3,94
EOS_GRUNEISEN	S1	S2	S3	GAMA	A	E0	V0			
	1,49	0	0	2,02	0,47	0	1			

The behaviour of high-explosives can be characterized using the Jones-Wilkins-Lee (JWL) equation of state, which describes the pressure-volume relationship during a detonation process [68, 69]. The JWL equation of state is based on the Gruneisen equation of state and is adjusted using experimental data. It is important to note that the JWL equation of state neglects factors such as viscosity, conductivity, friction, and external forces like gravity. However, its practical nature and extensive experimental data make it advantageous over alternative equations of state for the simulation of explosive materials. The JWL equation of state can be mathematically expressed as follows:

$$p = A'\left(1 - \frac{w}{R_1 V^*}\right) e^{-R_1 V^*} + B'\left(1 - \frac{w}{R_2 V^*}\right) e^{-R_2 V^*} + \frac{wE}{V^*} \tag{3.7}$$

Where A, B, R_1, R_2 and ω are the materials constants, E_0 is the detonation energy per unit volume and V represents the relative volume. The corresponding parameters of the explosive used are listed in Table 3.3 [56].

Tabel 3.3: Material and EOS parameters of the explosive.

Explosive							
MAT_HIGH_EXPLOSIVE_BURN	RO [kg/m³]	D(m/s)	PCJ(Gpa)				
	1,4	7000	25				
EOS_JWL	A	B	R1	R2	OMEG	E0	V0
	8,524	0,1802	4,55	1,3	0,38	0,085	0

The air is modelled using the NULL material model. Additionally, a linear polynomial equation of state (EOS) is employed to relate the pressure P to the energy per unit volume E_0 as it shows equation 3.8.

$$P = c_0 + c_1 u + c_2 \mu^2 + c_3 \mu^3 + (c_4 + c_5 \mu + c_6 \mu^2) E_0 \tag{3.8}$$

The linear polynomial equation of state (EOS) can be employed to represent air, utilizing the gamma law EOS by setting all constants C to 0, with the exception of C4 and C5 as defined in [70]. All parameters assumed for air are presented in Table 3.4.

Tabel 3.4: Parameters used for air.

Air									
MAT_NULL	RO [kg/m³]	PC	μ						
	1,29	0	0						
EOS_LINEAR_POLYNOMIAL	C0	C1	C2	C3	C4	C5	C6	E0	V0
	0	0	0	0	0,4	0,4	0	0	0

3.2.3 Formation process of the EFP

The sequence of images presented in 3.3 illustrates the transformation process of the EFP. Initially, we observe the explosion in progress, eliminating the casing, followed by our liner transforming into the intended shape.

0 ms

0,04 ms

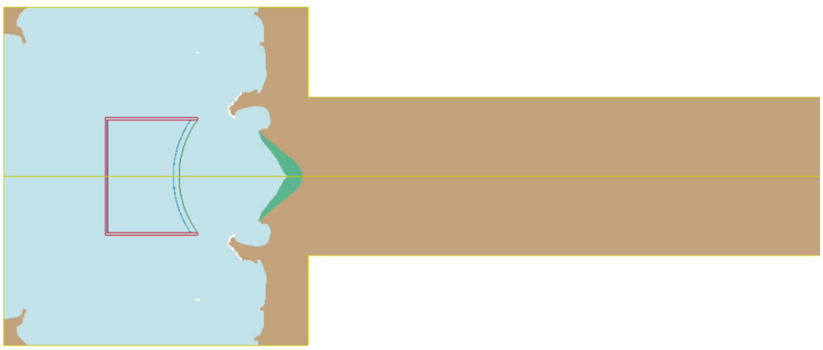

0,08 ms

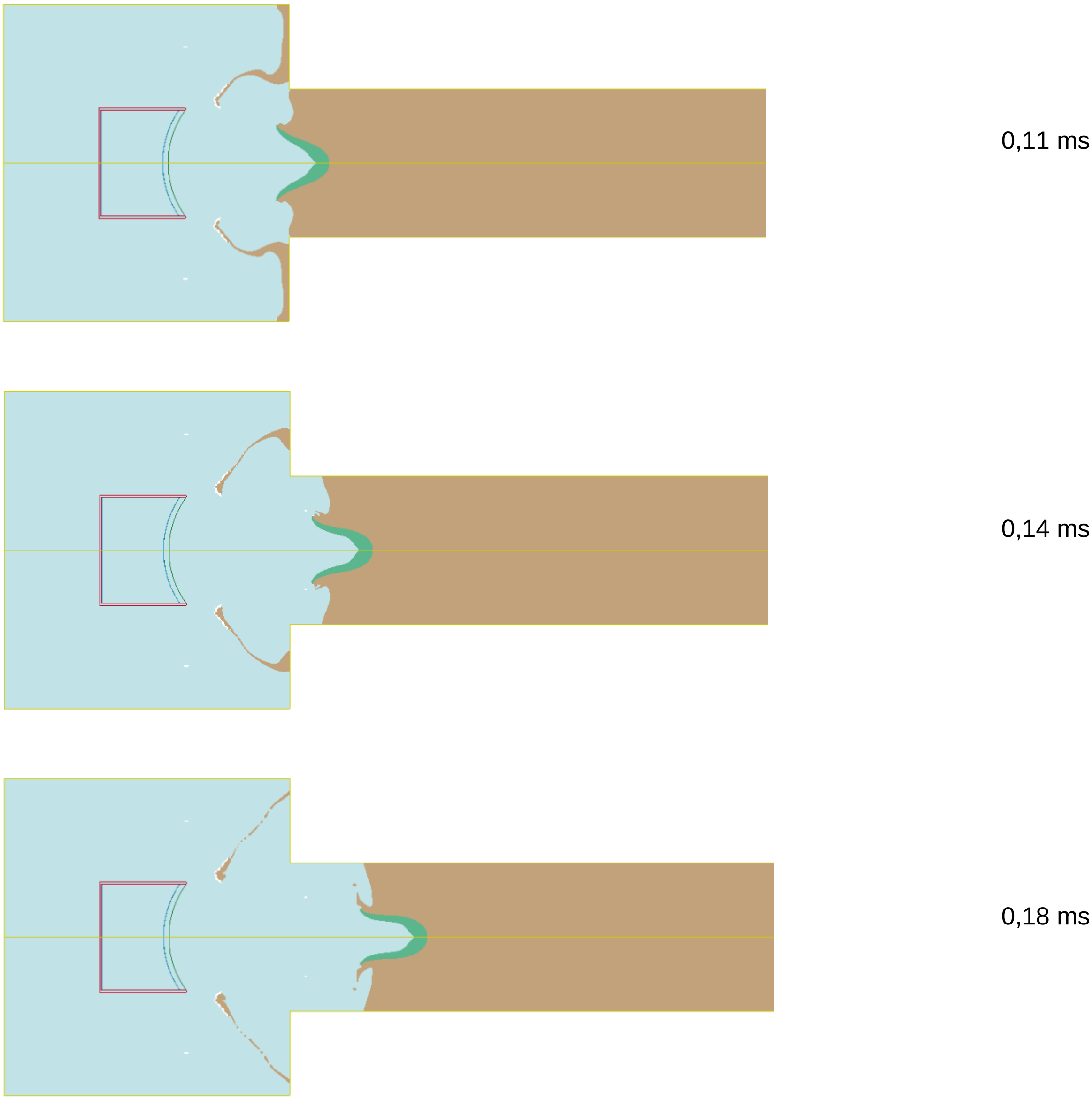

Figure 3.3: Sequence of EFP formation.

Figure 3.4 displays its attenuation velocity curve derived from the simulation, it can be observed that as the velocity of the EFP increases to 1223 m/s, there is a stable flying phase. The curve illustrates that the velocity process can be divided into two distinct phases. The first phase is the initial velocity phase, which spans until 0.12 ms, corresponding to the initial stage of formation where the head and bottom are not yet completely formed. The second phase is the stable flying phase, during which the EFP has fully formed and is flying steadily. In this period, the EFP encounters consistent air resistance, causing the velocity to decrease steadily, almost forming a straight line.

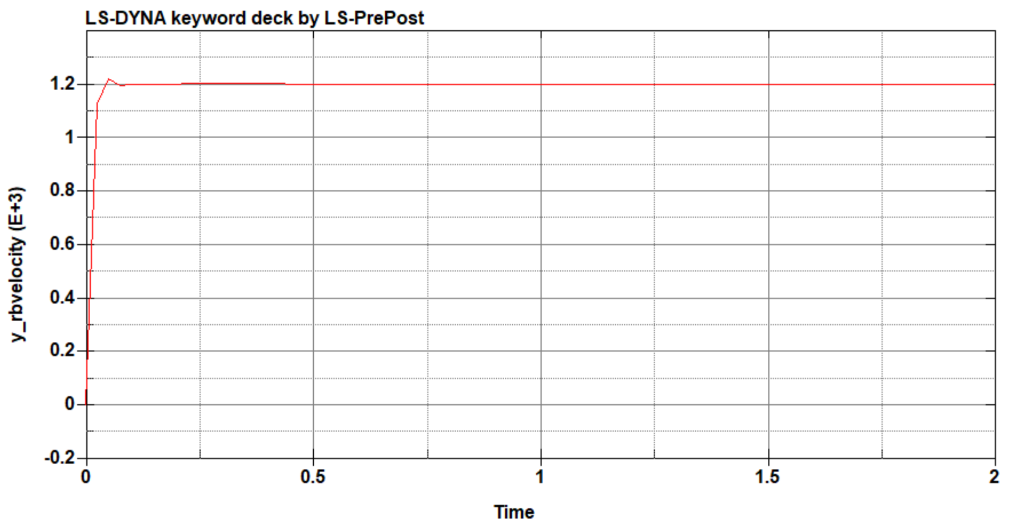

Figure 3.4: Velocity curve from the simulation.

4. Experimental campaign

For this dissertation, an experimental campaign was carried out at the Santa Margarida military camp with qualified military personnel responsible for handling, transporting, and storing the explosive materials in strict compliance with the safety regulations of the Portuguese Army.

This chapter delineates the various tests that were conducted, providing insights into their methodologies and procedures, as well as their underlying motivations. Subsequently, it presents the results obtained and offers a thorough analysis and interpretation of these findings.

4.1 Experimental procedures

4.1.1 EFP construction

The method used to construct the EFP involved adapting various parameters from previous research outlined in reference [46]. These parameters included the manufacturing process for the flyer plate, manufacturing of casing material and configuration, determination of the explosive charge weight, and calculating cap depth. In Figure 4.1, the design and schematic of the EFP can be observed. Table 4.1 presents the data of the corresponding EFP's that were produced.

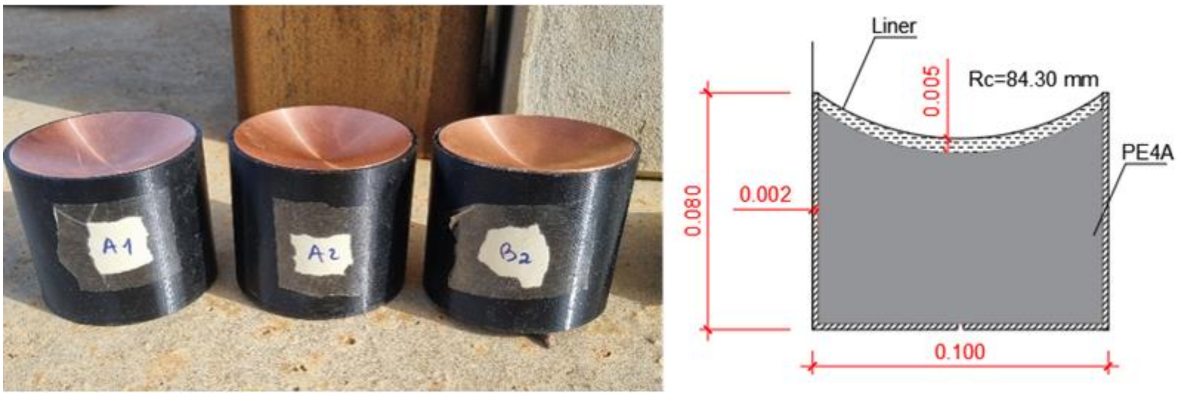

Figure 4.1: Design and schematic of the EFP.

Tabel 4.1: Data corresponding EFP's produced.

EFP Number	Mass [g]	Liner Weight [g]	Casing Weight [g]	Explosive Weight [g]
1	1127	354	117,5	655,5
2	1132,3	358,1	117,5	656,7
3	1127,2	357,5	117,5	652,2
4	1115,2	356,5	117,1	641,6
5	1118,6	345,1	117,6	655,9
6	1124,4	356	117,3	651,1
7	1120,9	358,2	117,1	645,6
8	1112,9	355,4	117,2	640,3

To create each individual flyer plate according to the desired shape and specifications, advanced computer numerical control (CNC) machining techniques were employed in the production of the liner. The machining process involved securing a solid copper block within the CNC machine, where precise cutting tools removed excess material to shape the liner to match the CAD model. Subsequently, the liner underwent additional post-processing steps including surface finishing, deburring, and thorough cleaning to attain the desired final appearance and smoothness. The resulting flyer plate measures 100 mm in diameter, 20 mm in height, and has an average weight of 355 grams. Figure 4.2 provides an illustration of a fully assembled flyer plate.

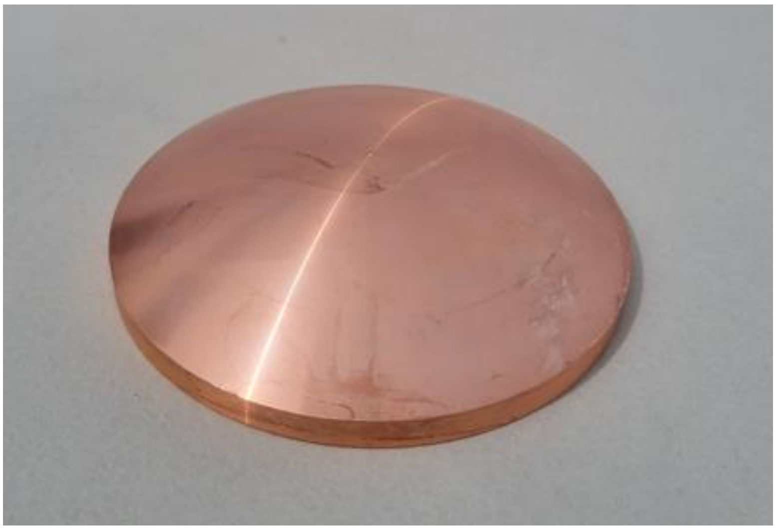

Figure 4.2: Flyer Plate.

The casing was manufactured using fused deposition modelling with an Original Prusa i3 MK3A 3D printer. For this purpose, PETG filament with a 1.75mm diameter was utilized, and it was extruded from the nozzle at a 0.4 mm diameter with a layer thickness of 0.3 mm. PETG, an acronym for polyethylene terephthalate glycol-modified, is a material created by combining PET (polyethylene terephthalate) with glycol. While PET is extensively used in various applications, it is not ideal for heating and extrusion processes due to its properties. To address this limitation, PET is precisely blended with glycol, resulting in PETG. The physical and mechanical properties of PETG, as documented by Coutinho [71], are summarized in the Table 4.2.

Tabel 4.2: Physical and mechanical properties of PETG.

	PETG
Density	1290 kg/m^3
Young's Modulus	1,5 Gpa
Poisson's ratio	0,33
yield strength	58 Mpa

In Figure 4.3, the left image showcases the 3D printer in action during the casing printing process, while the right image displays the completed printed casing.

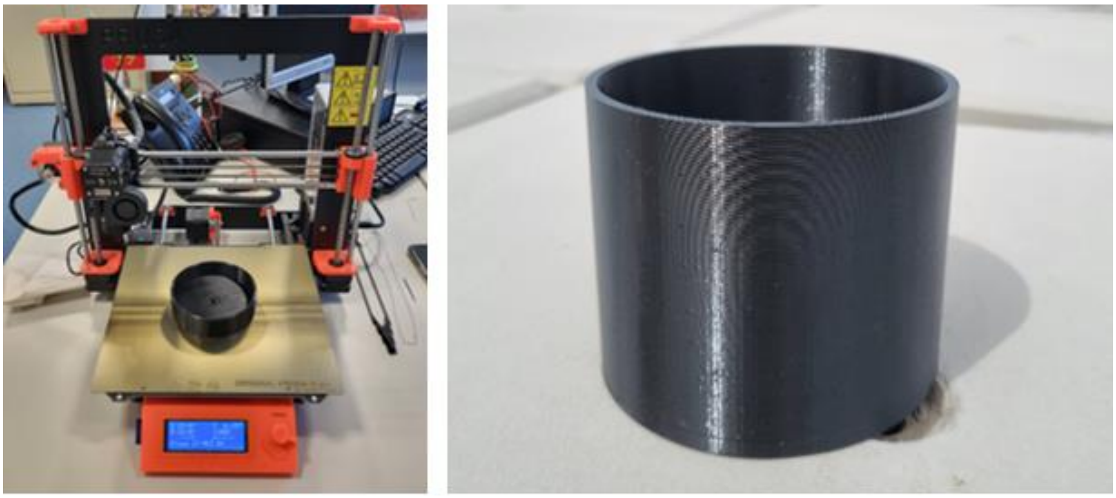

Figure 4.3: On the left side displays the process of 3D printing of the gradual construction of the casing. On the right side, the final result of the casing.

Once the casing and liner were prepared, the subsequent process was to load them with PEA4 explosive. On average, each casing was filled with 650g of this explosive material. The plastic explosive PE4A is hexogen based, with a detonation velocity of approximately 7000 m/s. It generally has a density of 1.4 g/cm3 and is usually presented in 230 g candles, as shown in Figure 4.4 [72].

Figure 4.4: Candle of PE4A [69].

The explosive material was carefully loaded into the casing, taking care to evenly compact it and avoid any voids or air bubbles. This left sufficient space for the liner to fit snugly in place. Figure 4.5, on the left illustrates the process conducted by the Portuguese Army´s Explosive Ordnance Disposal (EOD) team, showcasing the placement of the explosive material within the casing, the image on the right showcases the fully assembled casing with only the liner missing.

Figure 4.5: The image on the left depicts the EOD Team in the process of preparation, while the image on the right displays the fully assembled casing.

An electric detonator was consistently used in all tests. Electrical detonators employ an electric current to initiate an explosive charge. This type of detonator is highly reliable and can be precisely timed to ensure the initiation of the explosive charge at the desired moment. Finally, the detonation was carried out using a remote detonation system. Figure 4.6 displays the electric detonator and the wireless receiver.

Figure 4.6: Electric detonator and the wireless explosor.

4.1.2 Concrete Block Specifications

Each concrete block, as depicted in Figure 4.7, had dimensions of 600 mm x 600 mm x 400 mm with an initial volume of 0.114 m^3. The selection of these block dimensions took into account various considerations, including the availability of concrete forms, the lifting capacity of the equipment, and the anticipated penetration depth of the projectiles. To facilitate lifting, a small loop of rebar was embedded in the top middle of each block, allowing them to be easily handled using a forklift and chain. The blocks were not reinforced with any other materials.

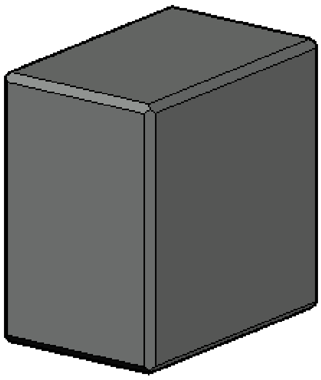

Figure 4.7: Concrete block.

The design specifications for concrete with basalt aggregate and limestone aggregate are presented in Table 4.3 and 4.4, respectively.

Tabel 4.3: Specifications for the concrete with basalt aggregate.

	Kg/m^3
Portland Cement, Type 1	320
Gravel, Basalt	572
Fine Basalt	469
Fine Aggregate	797
Adjuvant	2,5
Water	132

Tabel 4.4: Specifications for the concrete with limestone aggregate.

	Kg/m^3
Portland Cement, Type 1	324
Gravel, Limestone	588
Fine Limestone	468
Fine Aggregate	829
Adjuvant	2,67
Water	129

To obtain the concrete's compressive strength, three compression tests were conducted for each type of concrete (basalt aggregate and limestone aggregate). The cylindrical specimens had a diameter of 150 mm and a height of 300 mm. They were weighed to have a mass of 16 kg and a density of 2370.4 kg/m3.

For the basalt aggregate, the average compressive strength was 31.33 MPa. Figure 4.8 illustrates the evaluation of the concrete as the load was applied during one of the tests. All the results for the compression tests are presented in the annex A.

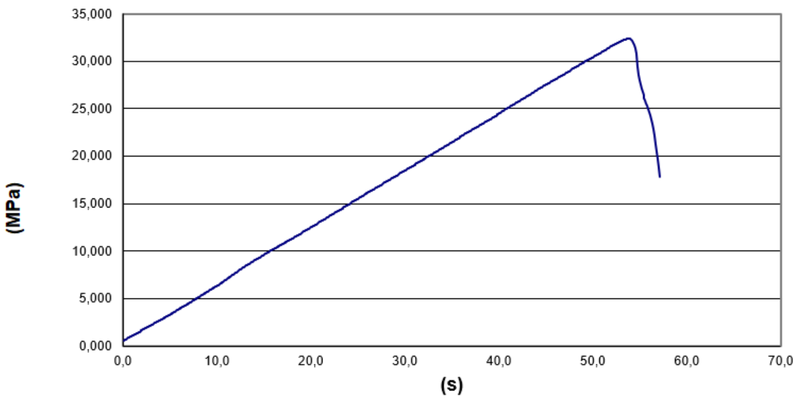

Figure 4.8: Evaluation of the concrete with basalt aggregate as the load was applied.

During the test, the cylindrical specimen was placed in a hydraulic compression machine. An increasing axial load was gradually applied until the specimen failed. Figure 4.9 showcases the different stages of the concrete cylinder, including its placement, the halfway point of the test, and the final result of the concrete.

Figure 4.9: Different stages of the concrete cylinder, including its placement, the halfway point of the test, and the result of the concrete.

Similarly, three compression tests were conducted for the limestone aggregate. The dimensions of the cylindrical specimens were identical to those used for the basalt aggregate.

During the compression tests, the specimens were subjected to increasing axial loads in a hydraulic compression machine until failure occurred.

The evaluation of the limestone concrete during the test is shown in Figure 4.10. The applied load and the resulting deformation of the specimens were monitored to determine the compression strength. After analysing the test data, the average compression strength of the limestone concrete was found to be 29.11 MPa, the limestone compression test sheets can be found in Annex B.

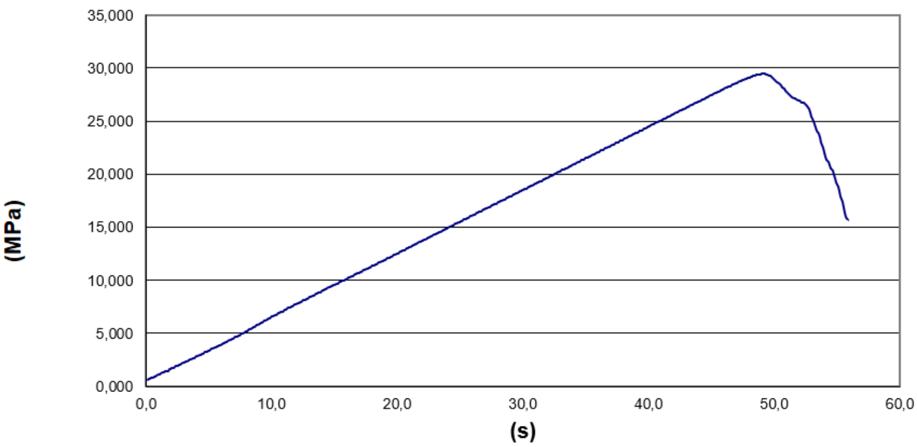

Figure 4.10: Evaluation of the concrete with limestone aggregate as the load was applied.

Figure 4.11 illustrates the process of the limestone cylinder, depicting its initial placement, and the final state of the concrete specimen after failure.

Figure 4.11: Initial placement, and the final state of the concrete specimen after failure.

4.1.3 Field Test Setup and Procedures

Figure 4.12 shows a side view of the set-up. The EFP was placed at a distance of 3.0 m because the simulation carried out in the previous chapter showed that the EFP was already fully formed and had a stable velocity.

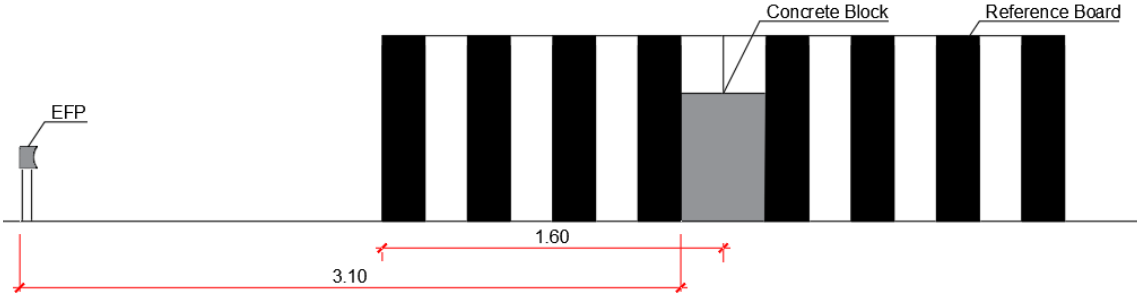

Figure 4.12: Side view of the set-up.

Figure 4.13 shows a plan view of the set up. The high-speed cameras have been left at a distance of 35.0 m for safety reasons so that no fragments can get close to them.

The concrete blocks were positioned on the ground and carefully levelled in both the front/back and left/right directions. The front face of the block was left free of any obstructions, such as gravel, ensuring a clear path for the EFP to impact, the sample was not confined in order to assess the projection of fragments.

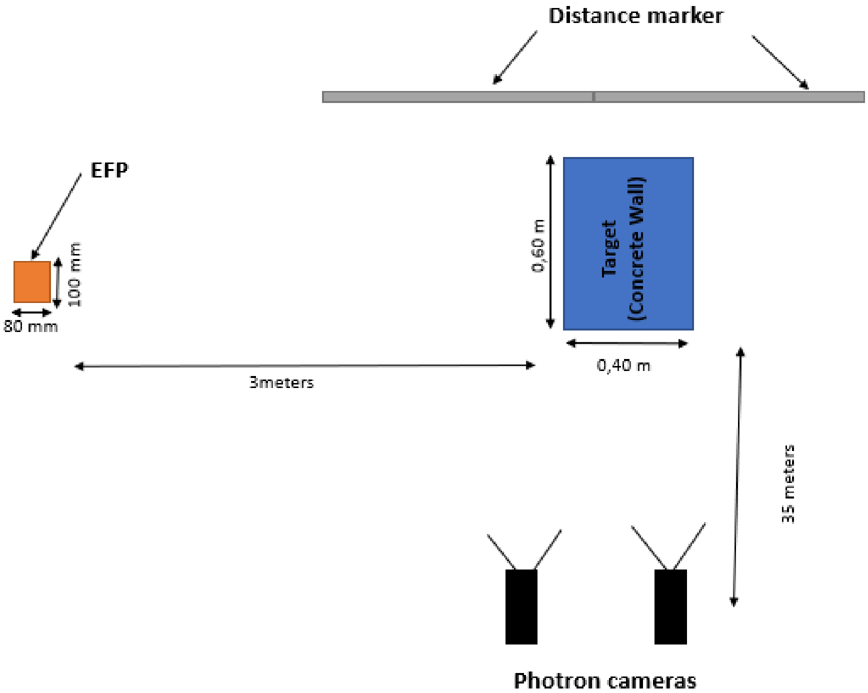

Figure 4.13: Plan view of the set-up.

Once the concrete blocks were in place, the impact face was painted black, while the opposite face was painted white. This was done to aid in the reconstruction process and to determine the orientation of the fragments. Figure 4.14 shows the process of the target placement.

Figure 4.14: Process of the target placement.

The support and placing of the EFP is an important component in ensuring the accuracy and effectiveness of the weapon. To ensure safety and precision targeting of the EFP, a disposable mount was employed. This cost-effective solution was preferred over other reusable systems.

In this experiment, a wooden frame was used as the support for the EFP. The frame had a hole at the top to allow for the EFP mount to be securely fastened in place. To ensure that the EFP was properly aimed at the concrete target, it was important to position the mount so that the height of the EFP was centred over the target. This helps to ensure that the projectile will be fired in a straight line towards the target. Figure 4.15 illustrates an EFP attached to the disposable support as well as the support after the detonation occurred.

Figure 4.15: EFP attached to the disposable support as well as the support after the detonation occurred.

To provide reference distances for velocity measurements, a reference board with 20 cm black and white stripes was placed within the camera's view. The board was 1.60 meters in length and was positioned perpendicular to the camera and parallel to the expected projectile trajectory. Figure 4.16 shows the camara view.

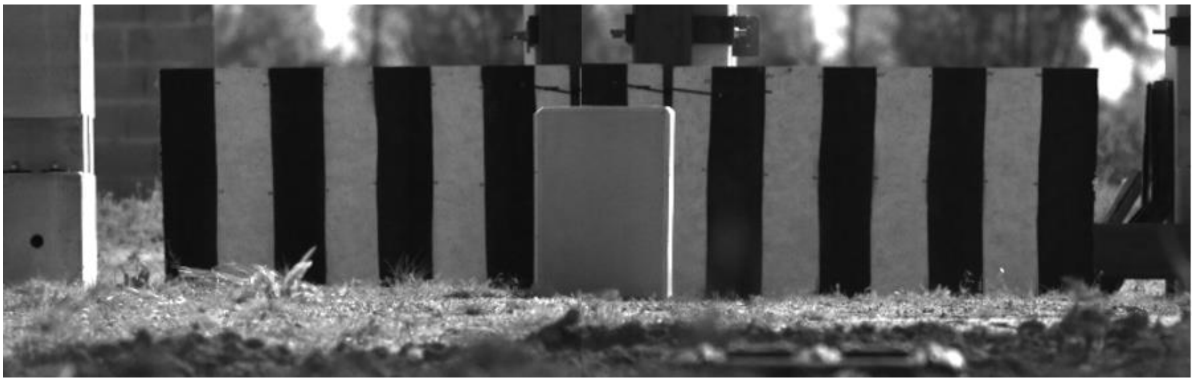

Figure 4.16: Camara view.

To ensure the safety of the camera system from potential air blast or fragments, it was positioned at approximately 35 meters from the concrete target. Ethernet cables were used to connect the camera to a laptop, enabling remote adjustment and triggering of the camera from a secure location during the tests. The specific camera settings for each shot were as follows:

- Lens type: Nikon
- Frames per second: 30000 fps
- Exposure time: 1.1 μs

- Resolution: 384 x 256

4.1.4 Laser Scanner

When this dissertation was being planned, the initial measure for measuring lost volume was to use a laser scanner to take an initial measurement of the concrete block and then take another measurement after the impact on the concrete. Unfortunately, the laser was too sensitive to light, since the tests were carried out in an open area and on sunny days it became difficult to carry out the measurements and it was not possible to get a good result with the laser. The model used was an Artec EVA laser as shown in Figure 4.17.

Figure 4.17: Model Artec Eva laser.

4.1.5 Concrete Volume and Crater Depth Measurements

Consequently, to quantify the volume of concrete loss resulting from the impact test, a specific procedure was implemented. After subjecting the concrete block to the test and fragmenting it into multiple pieces, each individual piece was weighed using a weighing scale.

To determine the volume, the recorded weights were then converted to volume units. This conversion was achieved by utilizing the known density of the concrete material used in the experimental campaign. The initial volume of the concrete block before the impact test was determined prior to the experiment. Subsequently, after the impact had occurred and the concrete block was fragmented, the individual volumes of the resulting concrete pieces were measured, only blocks with a diameter greater than 15 cm were considered for weighing, below this value was considered a loss due to crushing. The difference between the initial volume and the sum of the measured volumes of the concrete pieces provided valuable insights into the extent of volume loss caused by the impact.

This method of measuring the concrete volume following the impact test allowed for a quantitative assessment of the damage inflicted upon the concrete block. By quantifying the volume loss, it became possible to evaluate the effectiveness of the impact and understand the structural response of the concrete material.

The reconstruction process involved carefully assembling the fragmented concrete pieces to recreate the original shape of the block as closely as possible. This allowed for a more accurate assessment of the impact and the subsequent formation of the crater. Following the reconstruction, the depth of the crater was measured using a ruler.

4.2 Experimental Results

In this section, the details of each test carried out are presented, along with the results obtained in each one. It should be noted that the first 4 tests were carried out with basalt aggregate and the next 4 with limestone aggregate. After the presentation of each test, the conclusions of the experimental campaign are presented.

4.2.1 First Block

In the initial experiment, the EFP was positioned 3.10 m away from the concrete block. Upon impact at the centre, the concrete block broke into seven large blocks, while the smaller fragments were disregarded. Fragments of the concrete block were discovered at a maximum distance of 6.434 m. After weighing the individual blocks, the block lost 0.051 m^3 of its volume, which represents a loss of 35%. Figure 4.18 shows the display of the concrete block after the impact.

Figure 4.18: Display of the concrete block after the impact.

In the initial test, the penetration depth measured 20.27 cm. However, concrete surfaces had not been painted, making the reconstruction of the concrete block more challenging and, consequently, affecting the accuracy of the penetration value determination.

Through the use of high-speed cameras, the velocity of the projectile was measured to be 1166.96 m/s. In Figure 4.19, the left image captures the precise moment when the projectile makes contact with the concrete block, while the right image reveals visible scabbing and cone cracking.

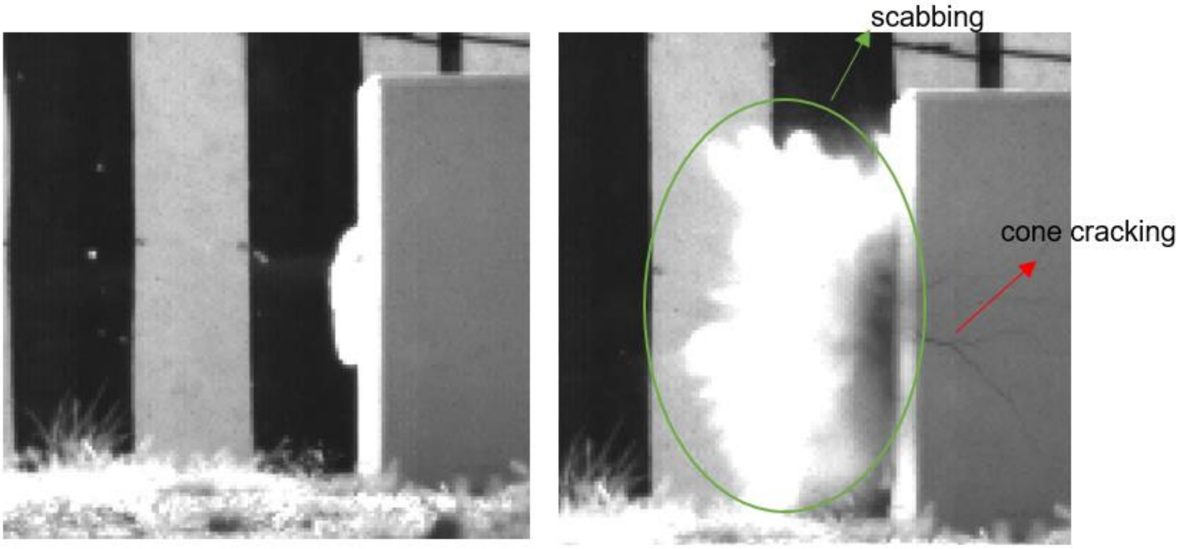

Figure 4.19: Frames of the high-speed cameras with the precise moment when impact occurs.

4.2.2 Second Block

In the second test, the shot was deviated 12.00 cm to the left and the EFP had a velocity of 1147.55 m/s. The EFP was positioned 3.10 m away from the target. In this test the fragments were found at most at a distance of 3.94 m away from the target and the fragments found at the impact site were formed by 3 large blocks. After the impact, the final volume was 89% of the initial volume, it's also possible to note that the scabbing crater was formed with a radius of 19.60 cm. Figure 4.20 shows the block after the impact.

Figure 4.20: Block 2 after the impact.

Due to the shot deviation, the penetration in this test was reduced, with a penetration depth of 12.36 cm before the shot escaped to the left. On the backside of the concrete block, where the shot deviated, only cracks formed, measuring 36.97 cm in length. On the opposite side where the projectile escaped, a crack of 24.72 cm was observed. Both cracks are showed in figure 4.21.

Figure 4.21: Visible cracks on the block after the impact.

4.2.3 Third Block

In this test, the shot was aimed almost directly at the centre of the concrete block, which was located at a distance of 3,10 meters from the firing point. After the impact, the concrete was completely destroyed; as shown in Figure 4.22. The impact resulted in the formation of seven large blocks, each varying in size and shape. Fragments were found at a maximum distance of 5.54 meters. High-speed cameras recorded a projectile speed of 1124.78 m/s.

Figure 4.22: Block 3 after impact.

To better understand the behaviour of the concrete, the block was reconstructed, as shown in figure 4.23. An impact crater of approximately 20.0 cm was observed, with a penetration depth of 19.65 cm into the concrete. Block 3 showed a volume loss of 38.68% of its initial volume.

Figure 4.23: Block 3 after reconstruction, front (left) and back (right) side.

In Figure 4.24 it's possible to witness the projectile approaching the block, followed by the initial contact between the projectile and the concrete block. Subsequently, we observe the scabbing process, ultimately leading to the formation of the cracking cone.

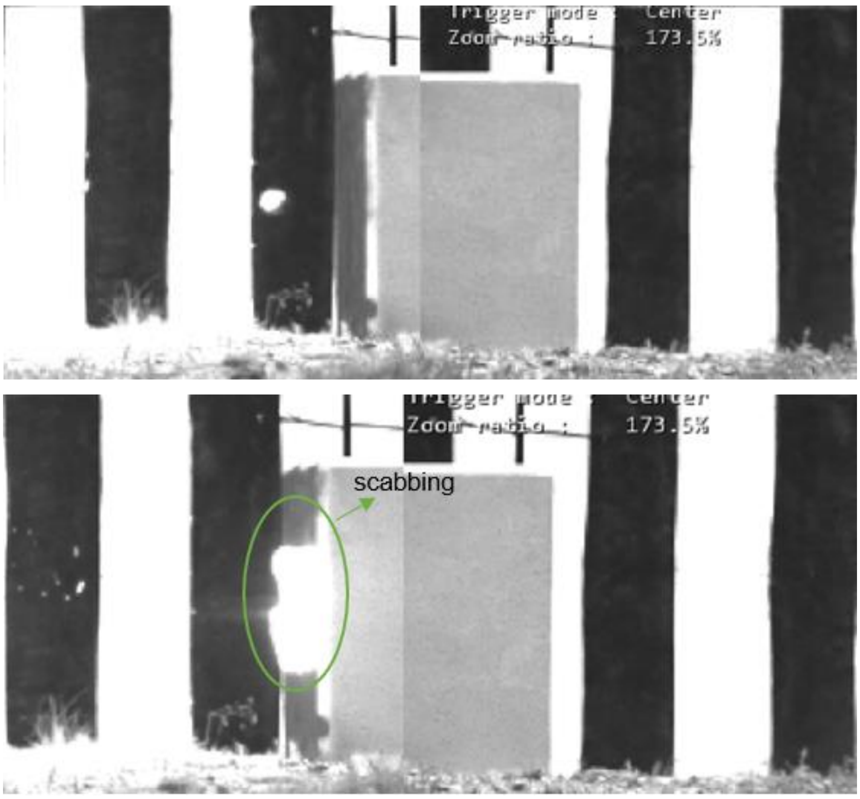

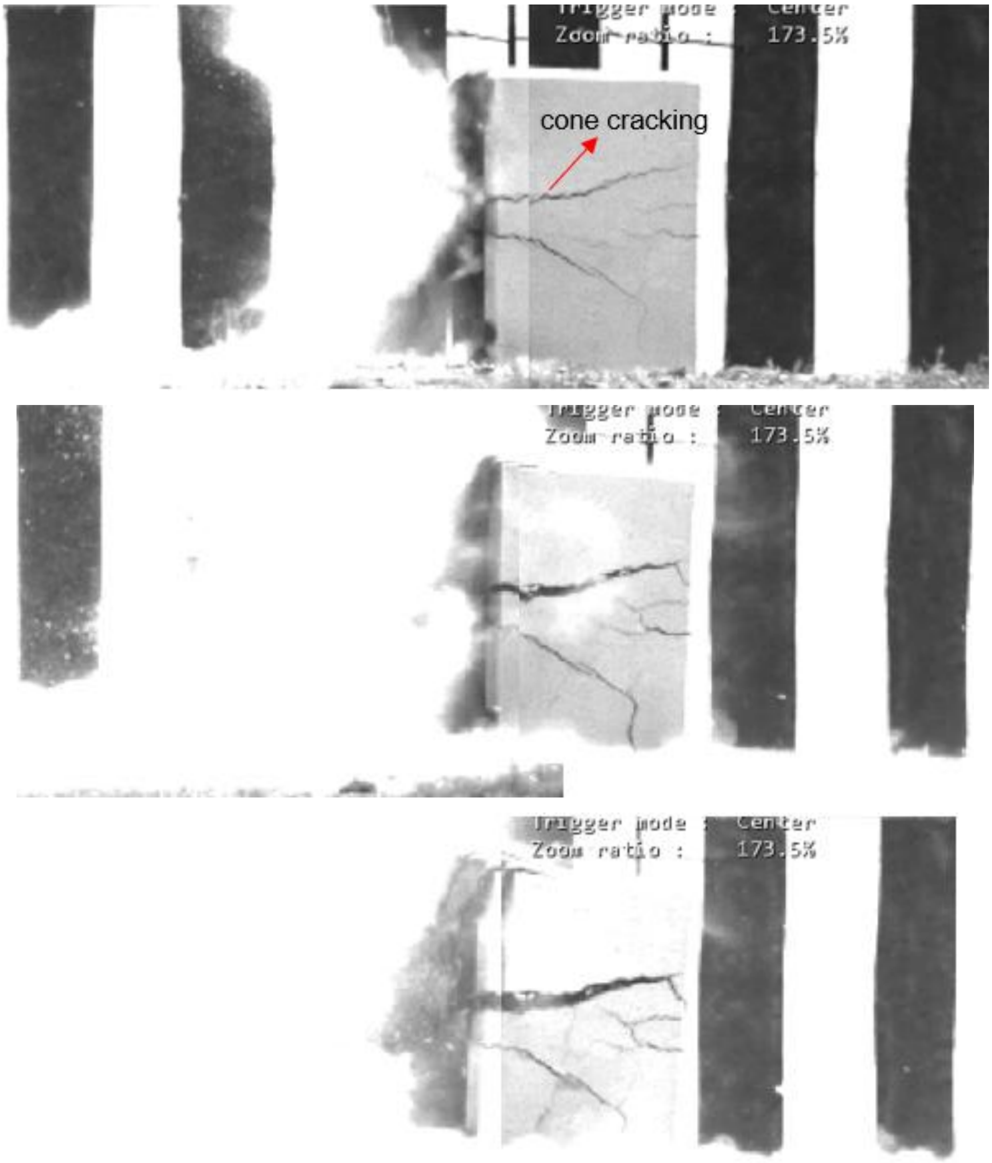

Figure 4.24: Sequence of the impact through the high-speed cameras.

4.2.4 Fourth Block

In test number 4, the results were quite similar to the previous test, although in this test, the shot was slightly deflected downward (6 cm) and to the left. In Figure 4.25 displays the concrete block after the impact.

Figure 4.25: Block 4 after the impact.

After the impact, the block was reconstructed as can be seen in figure 4.26, where on the left is a front view and on the right a side view of the concrete block. The rest of the concrete that formed the block shattered into pieces too small to easily recover and piece back together.

Figure 4.26: Front and side view of the block after reconstruction.

In this test, the EFP was placed at a distance of 3.10 m from the concrete block target. Upon impact, the EFP created six large blocks, with the fragment that travelled the farthest being found at a distance of 5.31 m from the target. Through the high-speed cameras, we obtained a speed of 1150.9 m/s. The reconstruction of the concrete block revealed a crater with a width of 18.36 cm and a penetration depth of 19.45 cm. In this test, the block lost 44.58% of its initial volume.

The series of images presented in Figure 4.27, captured by a set of GoPro cameras, illustrates the initial impact on the concrete block, followed by the progressive fracture process until complete separation occurs.

Figure 4.27: Sequence of frames of EFP impacting the concrete block.

4.2.5 Fifth Block

The fifth test introduced the use of limestone aggregate. The EFP was positioned at a distance of 3.10 meters from the concrete block, and fragments were found at a distance of 7.23 m. This impact resulted in the formation of 12 smaller blocks and a greater dispersion of fragments. Figure 4.28 illustrates the result after the impact.

Figure 4.28: Block 5 after impact.

Due to the smaller fragments resulting from the use of granite aggregate, reconstructing the concrete block became more challenging, as depicted in Figure 4.29. Nonetheless, through the reconstruction, it was possible to determine a penetration depth of 23.47 cm. After weighing the individual blocks, it was concluded that the volume loss was 53.4%. High-speed cameras recorded a projectile velocity of 1128.46 m/s.

Figure 4.29: Reconstruction of the block after impact.

4.2.6 Sixth Block

In this test, the EFP was positioned 3.12 m away from the target. The shot was fired at a slight upward angle, approximately 5.0 cm above the horizontal plane. Figure 4.30 displays the concrete block after the impact and its subsequent reconstruction.

Figure 4.30: Block 6 after the impact and its subsequent reconstruction.

The EFP achieved a penetration depth of 24.64 cm into the concrete block and the maximum distance of the fragments was 15.47 meters. Due to the upward angle of the shot, the fragmentation of the concrete was more pronounced at the top of the block, while the bottom part of the block was less fragmented, resulting in a volume loss of 29.1%. However, it is worth noting that the fragmented pieces were very small. Figure 4.31 shows an upper view of half of the block.

Figure 4.31: Upper view of half of the block.

From the high-speed cameras, a velocity of 1086.43 m/s was measured, and it was observed that the shot travelled in an upward trajectory, as shown in Figure 4.32.

Figure 4.32: Trajectory of the projectile.

4.2.7 Seventh Block

For this test, the EFP was placed at a distance of 3.1 m from the target. The shot was precise and resulted in the formation of thirteen fragments of the concrete block, as depicted in figure 4.33. An interesting observation from this test was that the farthest fragment was found at a distance of 21,74 m from the target.

Figure 4.33: Block 7 after impact.

The concrete block exhibited a higher degree of fragmentation compared to previous tests, making its reconstruction challenging, as shown in Figure 4.33. The possible reconstruction is presented in figure 4.34, which allowed for the determination of a penetration depth of 23.82 cm. In this particular test, a projectile velocity of 1129.91 m/s was recorded, the volume loss in this test corresponded to 54.58% of the initial volume.

Figure 4.34: Reconstructed block top view.

4.2.8 Eighth Block

In this test, the shot was slightly deviated to the right, resulting in the block being cut in half, as shown in Figure 4.35. The EFP was positioned at a distance of 3.10 m from the target, and the maximum distance where fragments were found was 12.76 m. With the high-speed cameras, a velocity of 1144.83 m/s was obtained. After the impact, the volume loss represented 47.01% of the initial volume.

Figure 4.35: Block 8 after impact.

The penetration depth was 21.04 cm, and on the side where the concrete didn't split, a crack was formed with a length of 40 cm. Figure 4.36 illustrates the damaged side of the concrete and the opposite side.

Figure 4.36: Damaged side of the concrete and the opposite side.

4.3 Experimental Conclusions.

Table 4.5 shows a summary of all the experimental results obtained.

Tabel 4.5: Experimental results obtained.

Test	Velocity [m/s]	Distance [m]	Penetration [cm]	Max dist of fragments [m]	Remaining Volume [m^3]
1	1166.96	3.09	20.27	6.43	0.0931
2	1147.55	3.09	12.36	3.94	0.1284
3	1124.78	3.1	19.65	5.54	0.0883
4	1150.9	3.09	19.45	5.31	0.0798
5	1128.46	3.1	23.47	7.23	0.0671
6	1086.43	3.12	24.64	15.47	0.1021
7	1129.91	3.09	23.82	21.74	0.0654
8	1144.83	3.1	21.04	12.76	0.0763

Graph 4.1 displays a velocity/penetration dispersion graph, with basalt values represented in red and limestone values in blue.

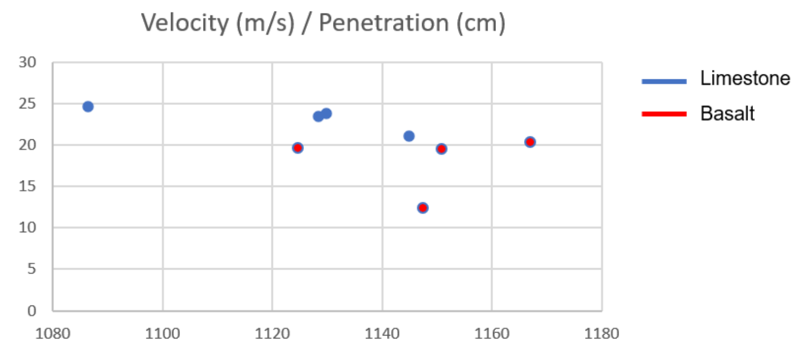

Graph 4.1: Velocity/ penetration dispersion graph

Upon analysing the data from all the experiments, several conclusions can be drawn. Firstly, the velocity values obtained showed no significant difference, indicating consistent velocities throughout the experiments. Similarly, a consistent distance travelled by the projectile was maintained across all tests. The measured speed was compared with the speed estimated by the Gurney equation as shown in Table 4.6 where it can be seen that the error is quite high, maybe this error came because the gurney equation assumes idealized conditions, such as uniform energy distribution and neglects factors like confinement, initiation, or energy losses.

Tabel 4.6: Comparison of the velocity measured with the Gurney equation.

Measured Speed (m/s)	Gurney Equation (m/s)	Error (%)
1166,96	1855	37,09%
1147,55	1853	38,07%
1124,78	1851	39,23%
1150,9	1847	37,69%
1128,46	1860	39,33%
1086,43	1852	41,34%
1129,91	1848	38,86%
1144,83	1847	38,02%

The measured velocity is also contrasted with the velocity provided by the numerical model discussed in Section 3.2, revealing a remarkable similarity, and emphasizing the significance of numerical simulations. Table 4.7 delineates the comparison between these two values and the corresponding error.

Tabel 4.7: Comparison between measured speed and numerical model speed.

Mesure Speed (m/s)	Numerical Model Speed (m/s)	Error (%)
1166,96	1223	4.65%
1147,55		6.20%
1124,78		8.08%
1150,9		5.97%
1128,46		7.75%
1086,43		11.18%
1129,91		7.63%
1144,83		6.45%

Examining the penetration data revealed that limestone aggregate exhibited higher penetration compared to the basalt aggregate tests. Although the strength of the two types of concrete blocks was similar, they showed different penetration results, as explained in Subsection 2.2.1 behaves differently for static and dynamic tensile loads in quasi-static actions, the material disperses energy through the weakest part because the force is applied slowly. In this scenario, the force takes a path around the aggregate and through the mortar. Conversely, in cases of high-velocity impact, the force is so rapid that it breaks through the middle of the aggregate. When it penetrates the aggregate, it dissipates more energy as the aggregate is more rigid. Due to higher hardness [71], the use of basalt aggregates improved penetration resistance, thus dissipating more energy.

The equations presented in Section 2.5 which predict the penetration depth of projectiles into concrete rely on a combination of variables, including concrete compressive strength, projectile weight or mass, calibre radius head (CRH), nose shape, projectile diameter or radius, and striking velocity. Since we were unable to retrieve precise data for our specific projectile, such as its weight, diameter, and calibre radius head, we have approximated these values based on previous studies that have investigated projectile recovery [43,48].

Table 4.8 not only presents a comparison between the measured penetration depths and the predicted values but also provides a contrast between the measured depths and the outcomes derived from seven different formulas. Within the "% dif" row, a negative value suggests that the formula resulted in an under-prediction of the penetration depth, while a positive value indicates an over-prediction.

Tabel 4.8: Comparison between the measured penetration depths and the predicted values.

Block	Experimental Penetration Depth [cm]	Modified Petry Formula [cm]	Modified NDRC [cm]	Amman and Whitney [cm]	Whiffen [cm]	Kar [cm]	Forrestal 1994 [cm]	UFC 3-340-02 [cm]
1	20,27	32,5	43,6	58,2	56,1	19,8	18,3	19,8
2	12,36	32,3	43,3	57,8	55,6	20,1	18,7	19,7
3	19,65	32,2	43,2	57,5	55,4	19,7	18,4	20,1
4	19,45	32,4	43,5	58	55,6	19,9	18,7	19,8
5	23,47	32,2	43,2	57,6	54,9	19,7	19,1	19,9
6	24,64	31,9	42,8	57,4	55,7	20,1	18,8	19,5
7	23,82	32,2	43,2	57,6	55,4	19,8	18,6	19,2
8	21,04	32,3	43,3	57,7	55,2	19,9	19	20,4
Average	20,6	32,3	43,3	57,7	55,5	19,9	18,7	19,8
Average %		56,7%	110,1%	180,1%	169,40%	-3,39%	-9,22%	-3,88%

Because the blocks utilized in this study were not cast within culverts, and the mentioned previous study does not provide guidance on how confinement around the targets could impact penetration depth, it's challenging to definitively ascertain how much the measured penetration depths might have deviated with wider blocks. Consequently, this disparity between the experimental outcomes and the formula-based results can be attributed to these factors and, in some instances, did not impact the centre of the concrete block.

Exploring the investigation into the maximum fragment distance, it was observed that employing limestone aggregate led to significantly greater distances in comparison to basalt aggregate. This disparity could be attributed to the comparatively smaller size of limestone fragments, which resulted in their projection to more distant locations, limestone fragmented into more and smaller pieces because there was more crushing. This could be related to the lower hardness of the aggregates. Notably, the farthest fragment recorded in these tests travelled a distance of 21.74 meters from the target. This finding underscores the potential danger posed by high-velocity impacts in real-world scenarios, as fragments may travel considerable distances and cause significant damage.

An additional conclusion drawn from these experiments is that the location of impact significantly influences the fragmentation pattern. When the impact occurs at the centre, fragmentation is observed in all directions. However, when the shot is deviated from the centre, the fragments tend to travel predominantly in the deviated direction, as depicted in Figure 4.37. This finding highlights the directional influence on the dispersal of fragments, indicating the importance of impact location in understanding the resulting fragmentation behaviour.

Figure 4.37: Fragments direction after impact.

Following each test, an examination was conducted to locate fragments of the EFP. The discovered fragments are depicted in Figure 4.38, where each quadrant represents a 2x2 cm area.

Figure 4.38: Fragments found of the EFP.

5. Numerical model analyses

Experimental campaigns have been conducted to investigate the behaviour of concrete structures under high-velocity impacts. However, these experiments are often limited in scope, expensive, and time-consuming. Therefore, complementing these experimental campaigns with numerical models is highly beneficial. Numerical models provide a more comprehensive understanding of the underlying physics and mechanics of these events. In this regard, a numerical model was developed to complement the experimental campaign.

The numerical model allows for a more detailed analysis of the behaviour of concrete structures under high-velocity impacts, enabling the investigation of parameters that are difficult to measure in experimental tests. In addition, the model can be used to study a wider range of impact scenarios, including those that are difficult to replicate in experimental tests.

5.1 FE numerical model

In the present study, a FE numerical model was developed to validate our experimental campaign and gain deeper insights into the behaviour of concrete under impact. This model faithfully recreates the experimental setup, including the concrete block and the surrounding environment. Since it was not possible to recover the EFP during the experimental campaign it had to be recreated based on existing literature, utilizing data from a previously recovered EFP [52]. To maintain uniformity in the units across all numerical models, the units outlined in Section 3.1 were consistently applied in this particular model. Figure 5.1 gives an overview of the numerical model..

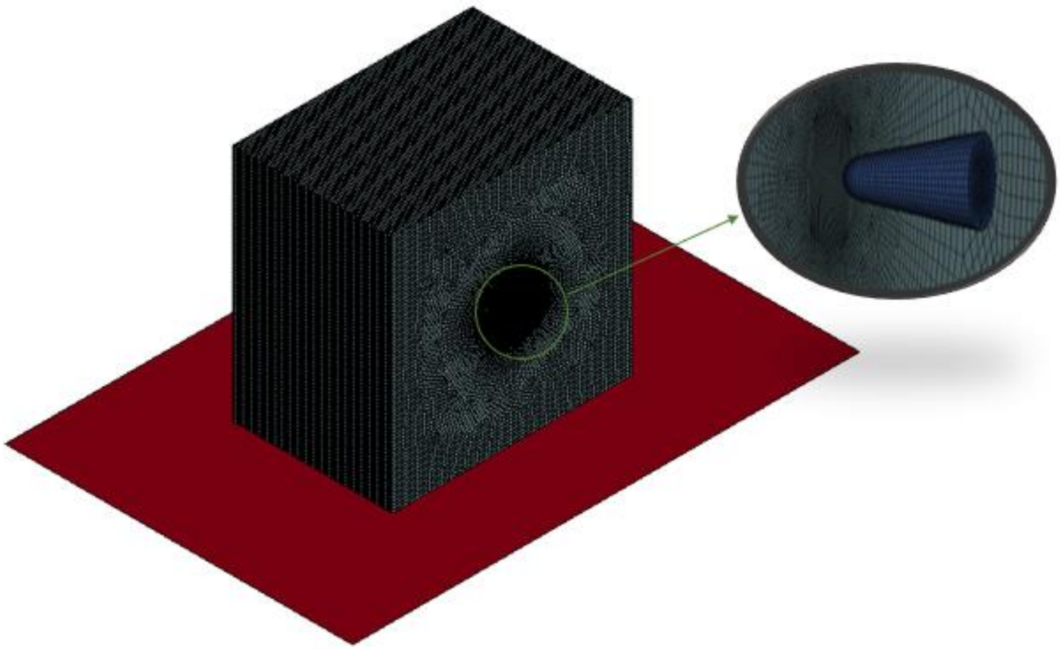

Figure 5.1: Overview of the numeric model.

5.1.1 Geometry and boundary conditions

The initial step involved defining the concrete block, which matched the dimensions of the block utilized in the previously described experimental campaign (Section 4.1.2). The concrete block was discretized using a progressive meshing approach, with mesh sizes decreasing towards the centre. Specifically, the mesh was divided into five sections, starting at 7.5 mm farthest from the centre, then progressing to 6.5 mm, followed by 5.5 mm, and then 2.7 mm and, lastly, 1.5mm. This method aimed to optimize the model's efficiency by reducing its overall computational effort while maintaining a highly detailed mesh in the impact zone. In Figure 5.2 one may observe the concrete block and the resulting mesh.

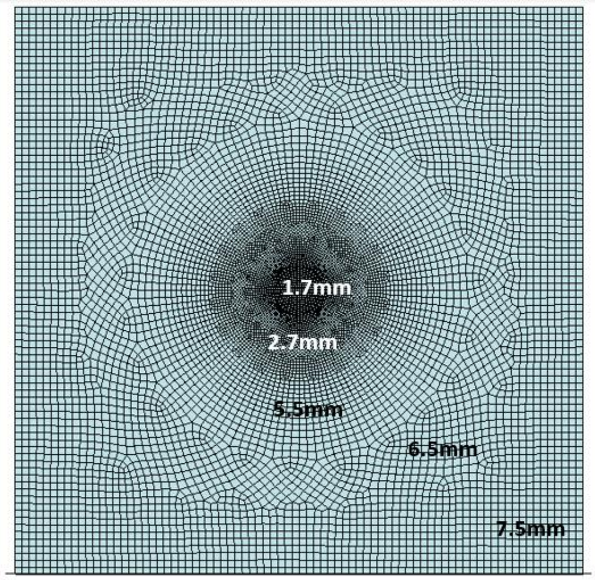

Figure 5.2: Concrete mesh.

The modelling of the EFP was followed by positioning it at a 5 cm distance from the concrete block to optimize simulation time, as the EFP's velocity exhibited minimal fluctuations along its trajectory. Initial velocity generation was utilized to set the initial velocity of the EFP to 1200 m/s, consistent with the speed specified in the numerical model for EFP creation.

The EFP’s geometry was created in the Fusion 360 program and then uploaded to LS-DYNA to create the mesh. Subsequently, the floor was generated using the rigid wall function available in LS-DYNA. For enhanced realism, the simulation incorporated gravitational acceleration acting upon the block, inducing pressure on the floor. Additionally, a coefficient of friction was established between the block and the floor to simulate their interaction more accurately.

As previously referred, constant stress solid elements were used to model both the concrete block and the EFP. Consequently, hourglass control was activated in order to avoid zero energy modes.

Additionally, in order to apply the load resulting from the detonation of the explosive charge, Load Blast Enhanced function was used. This load represents an air burst with ground reflection, generating a powerful blast effect with the use of 650g of PE4A explosives, equivalent to 840g of TNT. This load definition is essential in understanding the impact of the shock wave had on the concrete block. Additionally, an area of segments has been established for the precise application of the blast load pressure, namely the front face of the concrete block.

The interaction between the EFP, designated as the master, and the concrete, treated as the slave, was modelled using the Contact Eroding Surface-to-Surface approach. This method involved incorporating both static and dynamic coefficients of friction, each set at 0.2. Card A pinball segment based contact penalty formulation was activated, which allowed for adjustments in handling contact to account for varying stiffness properties. This ensured that the simulation accurately represented the influence of material stiffness on the interaction between the EFP and the concrete.

5.1.2 Material modelling

In this study, the material model 072_Concrete Damage REL3, commonly referred to as the Karagozian and Case Concrete model (KCC). This model is widely employed for simulating the behaviour of concrete structures [74,75]. It falls under the category of isotropic, plastic-damage, and rate-dependent models, providing a comprehensive representation of concrete material properties.

This material model, known as the KCC model, effectively captures the elastic behaviour of concrete using Hooke's law, ensuring a precise representation of concrete's linear elastic response [76]. One notable advantage of the KCC model is its simplicity in parameterization, as it automatically generates all the required parameters based on just one input parameter, the concrete's unconfined compressive strength [77]. Determining the unconfined compressive strength through experimental testing is a straightforward process, making the KCC model a valuable tool for simulating how concrete structures respond to blast and impact events.

Isotropic materials, like concrete, often employ stress invariant functions to establish their failure criteria. In this study, the concrete material's failure criterion is defined using stress invariants. The stress tensor, denoted as σ_{ij}, serves as the foundation for stress invariant functions, which comprise two components: the deviatoric stress tensor, s_{ij}, and the hydrostatic stress tensor, σ_{ij}. The general expression can be formulated as follows:

$$\sigma_{ij} = s_{ij} + \sigma_h \delta_{ij} \tag{5.1}$$

This model also considers damage and strain-rate effects. An Equation-of-State is essential to describe the pressure-volume strain response. The three failure surfaces in the KCC model are characterized by three sets of parameters: (a_0, a_1, a_2) for the maximum shear failure surface, (a_{0f}, a_{1f}, a_{2f}) for the residual failure surface, and (a_{0y}, a_{1y}, a_{2y}) for the yield failure surface. Compressive shear strength is typically determined using a triaxial compression test, with stress difference and mean stress plotted on a graph [78].

However, the Concrete Damage Model Rel3 has limitations in accurately simulating physical scabbing and spalling. To address this issue, an additional keyword, Mat Add Erosion, has been introduced to allow for failure and erosion in constitutive models that do not inherently support such behaviour. The Mat Add Erosion option offers multiple criteria for defining erosion and failure, which can be independently applied. During simulations, elements are deleted when one or more of these criteria are met. The present study used erosion of elements based on the maximum effective plastic strain.

While this material typically generates values automatically, we made certain adjustments to enhance the accuracy of the results. The initial modifications focused on the parameters b_1 and b_2. The automatically generated b_1 value is 1.60 for an element size of 60 mm. Given that our element size averages around 2.5mm, we recalculated our b_1 value using the expression provided in equation 5.2 where h represents the characteristics length of the element in mm. Consequently, we obtained a b1 value of 0.82 for our specific case.

$$b_1 = 00135h + 0.79 \tag{5.2}$$

Subsequently, the value of b2 was reevaluated. The material's default automatic value for b2 is 1.35, determined by an expression represented in equation 5.3, with parameters w_{lz} represents the localization width in millimetres, which is usually three time the maximum aggregate size and f_c' is the concrete strength in MPa. In our specific scenario, where w_{lz} equals 50 and fc is 30 MPa, the recalculated b2 value was found to be 1.19.

$$b_2 = (1.4 \times 10^{-4} w_{lz}^2 - 0.039 w_{lz} + 3.06)(0.516 - 8.4 \times 10^{-5} f_c'^2 + 0.014 f_c') \tag{5.3}$$

A study conducted by Fang and colleagues [79] explored the required modifications to adapt the 072 Concrete Damage REL3 material for impact scenarios. In this dissertation, some of these suggestions have been followed in relation to the strength surface parameters, these have been defined from the triaxial compression data of 45.4 MPa concrete and expressed as function of concrete compressive strength. The new expressions used are expressed below.

$$a_0 = 0.4426 f_c\,;\; a_1 = 0.5698\,; a_2 = 0.02516/f_c \tag{5.4}$$

$$a_{0y} = 0.2797 f_c\,;\; a_{1y} = 0.8989\,; a_{2y} = 0.0685/f_c \tag{5.5}$$

$$a_0 = 0\,;\; a_{1f} = a_1\,; a_{2f} = a_2 \tag{5.6}$$

Table 5.1 shows the values introduced into the concrete material.

Tabel 5.1: Values of concrete material.

<table>
<tr><td rowspan="6">Concrete</td><td>RO [g/cm³]</td><td>PR</td><td>A0</td><td>A1</td><td>A2</td></tr>
<tr><td>2,4</td><td>0,2</td><td>13,278</td><td>0,5698</td><td>8,38E-04</td></tr>
<tr><td>B1</td><td>Omega</td><td>NOUT</td><td>RSize</td><td>UCF</td></tr>
<tr><td>0.82</td><td>0,5</td><td>2</td><td>0.0393700</td><td>1,45E+05</td></tr>
<tr><td>Locwith</td><td>A0y</td><td>A1y</td><td>A2y</td><td></td></tr>
<tr><td>57</td><td>8,39</td><td>0,8989</td><td>2,28E-03</td><td></td></tr>
</table>

As referred in Section 3.2.2, the material used for the EFP model was the Johnson-Cook constitutive model. The values used were the same as those presented in the referred section.

5.2 Results

One of the parameters that greatly influenced the attained results was the maximum effective plastic strain parameter used in Mat Add ErosionConsequently, several values were used in order to verify its influence on the results. Figure 5.3 displays three model examples with varying values: the first image features a value of 0.15, the second 0.18, and the third 0.25, all frames were taken at the same time, 3.5 ms. Analysing the illustrated results, one may verify that, as expected, the maximum effective strain influences the concrete's ductility and the formation of large cracks. Note that, although not depicted, the model with a 0.25 maximum effective plastic strain is completely damaged where cracks have formed in the remaining models.

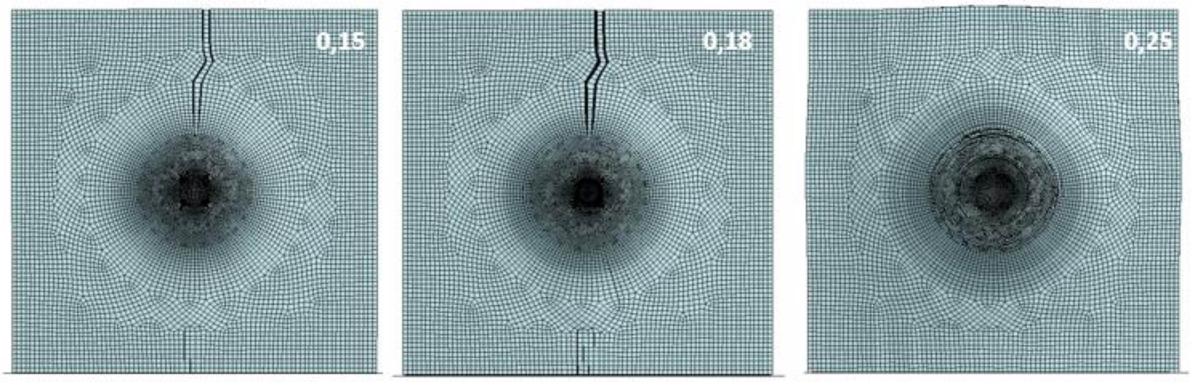

Figure 5.3: Differences between effective plastic strain values.

In graph 5.2 we can also see the different penetrations depending on the value of effective plastic strain.

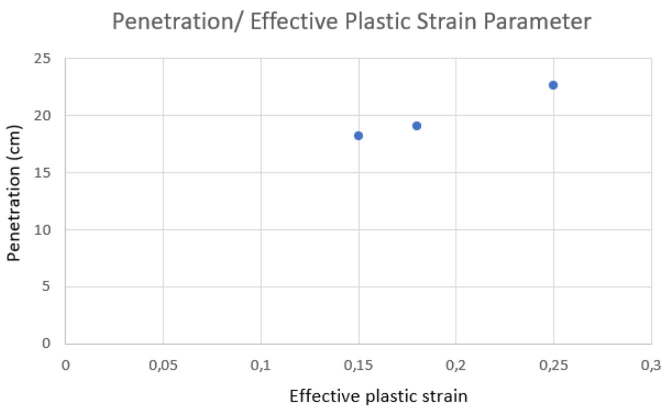

Graph 5. 1: Penetration differences depending on the value of effective plastic strain.

Comparing the model's results with those from the experimental campaign, we observe a penetration depth of 19.1 cm in the model, whereas the experimental campaign yielded an average value of 21.76 cm, showing a close resemblance. Figure 5.4 illustrates the projectile reaching its maximum penetration depth.

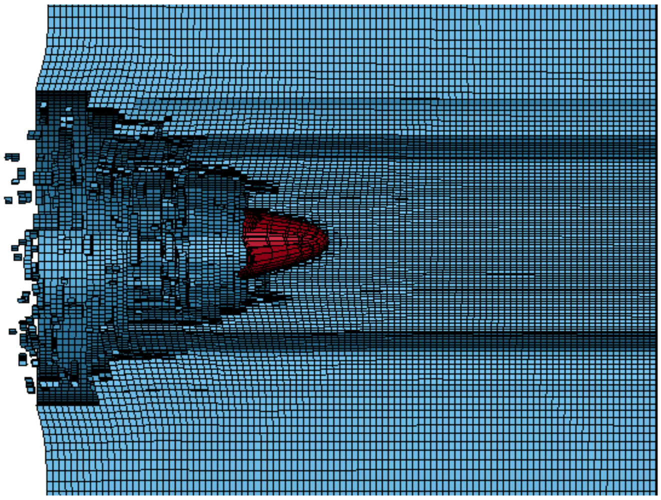

Figure 5.4: Projectile reaching its maximum penetration depth.

Another point of comparison with the experimental campaign is the crater formation. In the model, the crater measures 23 cm, whereas in the experimental campaign, it's 19 cm. Figure 5.5 provides a side-by-side comparison of the craters from the numerical model and the experimental campaign. Note that the numerical model’s figure illustrates the fringe of the attained damage, where blue corresponds to undamaged concrete and red depicts fully damaged concrete..

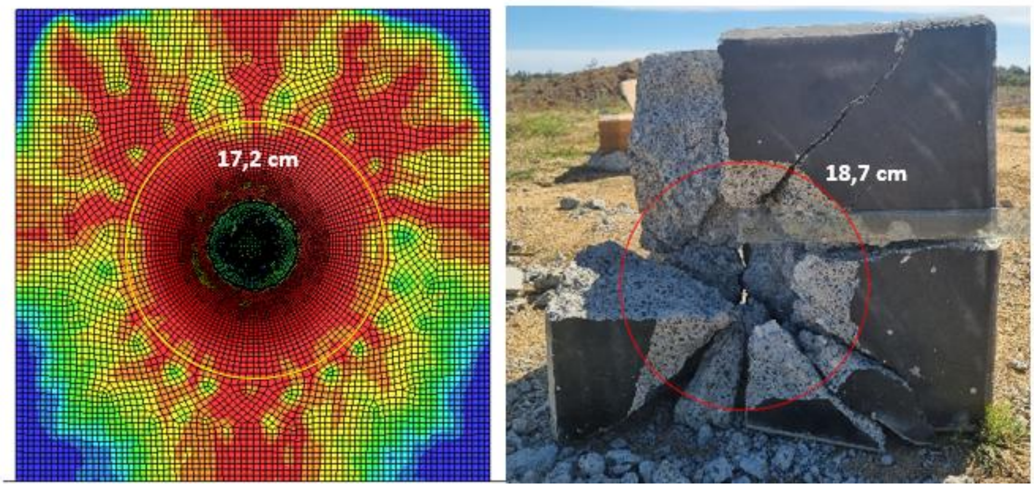

Figure 5.5: Comparison of the craters from the numerical model and the experimental campaign.

Figure 5.6 displays a series of images depicting the front face of the concrete block. These images illustrate the damage resulting from the impact. Initially, we observe the formation of the impact crater, followed by the emergence of cracks, and ultimately, the concrete block breaking apart.

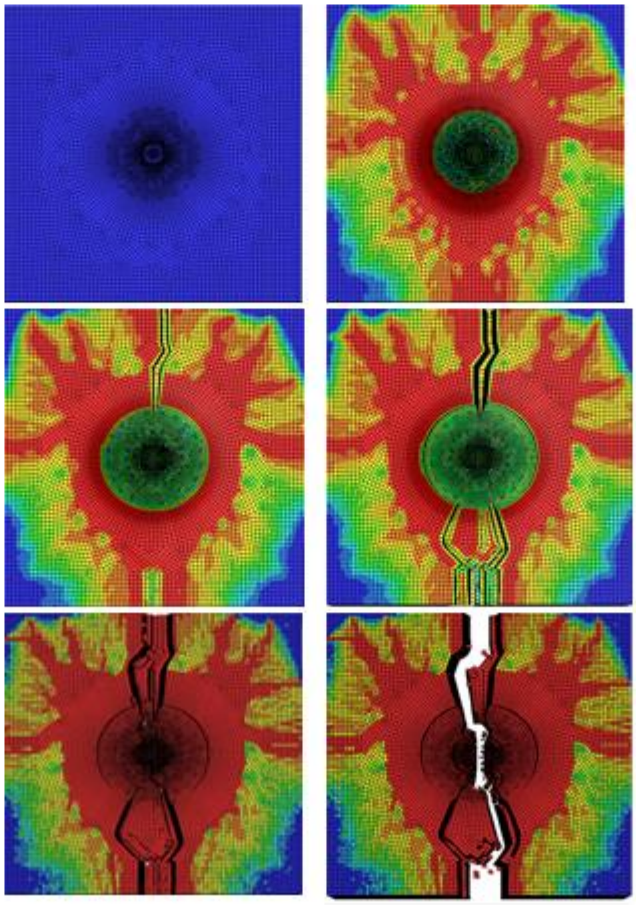

Figure 5.6: Impact sequence.

6. Conclusions

6.1 Synthesis and main conclusions

In conclusion, this dissertation has explored the concrete behaviour under high-velocity impacts, an area of study that has garnered increasing attention in recent times. The central goal of this research was to shed light on the behaviour of concrete structures when subjected to high-velocity impacts.

This journey began with the development of a numerical model, which was used to design the EFP so that it would reach a speed greater than 1000 m/s. This endeavour was fruitful, as the numerical model predicted a velocity of 1223 m/s, closely aligning with the real-world scenario where we observed a velocity of 1135 m/s. This alignment not only validated our simulation approach but also affirmed the reliability of the EFP in reproducing high velocity conditions.

While there was an initial discrepancy between the velocity attained resorting to empirical formulas and the experimental results, this discrepancy highlights the importance of such studies in formulating new, more reliable formulas for high-velocity impacts. However, it's worth noting that the high-speed images captured during our experiments were consistent with our modelling, demonstrating the significance of these numerical observations.

During our field campaign, we conducted experiments using two different types of concrete blocks: one utilizing basalt aggregate and the other limestone aggregate. These tests produced invaluable data, revealing differences in behaviour between the two types of aggregates. The harder, basalt aggregates, exhibited greater energy dissipation capacity, resulting in reduced penetration and the formation of craters, as compared to the limestone aggregates. Comparing these results between the basalt and limestone blocks highlights the implications of aggregate choice in designing structures for high-velocity impact resistance.

The experimental campaign also enabled us to verify and observe the formation of different failure mechanisms in concrete, in accordance with existing literature. This contribution is significant, as it aids in the study of protective solutions and strategies to mitigate the effects of high-velocity impacts, thereby enhancing the safety of structures and infrastructure in extreme events.

The importance of numerical modelling cannot be overstated in this research. Initially, a 2D numerical model was developed to simulate the EFP, and later, a comprehensive 3D numerical model that incorporated the EFP and the impacted concrete block. These models played a crucial role in validating our experiments and provided insights that were not directly measurable in the field. The alignment between the values obtained from our experiments and the numerical models underscores the importance of this approach in saving resources and providing more efficient methods for studying high-velocity impacts.

The significance of this work extends beyond academic curiosity. Understanding how concrete responds to dynamic loading is essential for the design of resilient structures that can withstand extreme events, including earthquakes, explosions, and high-speed impacts. By advancing our comprehension of concrete's behaviour under such conditions, we can pave the way for more efficient materials and structures, thus mitigating the risk of catastrophic failure and enhancing safety in the face of extreme events. This research contributes to the ongoing efforts to create a safer and more robust built environment.

6.2 Recommendations for the future

The goals of this thesis were effectively accomplished. Throughout the research, we pinpointed areas with potential for improvement:

- The use of a stake as a EFP support proved to be more labour-intensive than anticipated. Therefore, considering an alternative support like a tripod might be more efficient, with a tripod the EFP could easily be aligned precisely with the target;
- A solution for recovering the projectile should be explored. This would provide accurate dimensions and weight for replication in the numerical model, enhancing precision.

For future work, some research topics of interest were also identified:

- Study the difference in results using a shaped charge instead of EFP;
- Incorporate materials into the concrete to enhance its protective qualities, examine their performance under impact, and analyse the disparities in penetration;
- Run the simulation in 2D and see if the penetration depth varies much from that of the 3D model.

References

[1] Jenkins, B. (2006). The New Age of Terrorism. In The McGraw-Hill Homeland Security Handbook (pp. 117-130).

[2] Esteban, B., Lenhart, L, et al. (2015). An Evaluation of Shaped Charge Experiments Using Concrete Components. International Journal of Protective Structures, 6(3), 439–455. https://doi.org/10.1260/2041-4196.6.3.439

[3] Schneider, E., & Schäfer, F. (2001). Hypervelocity impact research - acceleration technology and applications -. Advances in Space Research, 28(9), 1417–1424. https://doi.org/10.1016/s0273-1177(01)00448-3

[4] Meyers, M. (1994). Dynamic Behavior of Materials. Wiley, New York. https://doi.org/10.1002/9780470172278

[5] Leppänen, J. (2005). Experiments and numerical analyses of blast and fragment impacts on concrete, International Journal of Impact Engineering, 31, 843–860. https://doi.org/10.1016/j.ijimpeng.2004.04.012

[6] Gebbeken, N., Teich, M. (2007). Numerical modelling of high-speed impact and penetration into concrete structures. In F. L. Huang, Q. M. Li, & T. S. Lok (Eds.), Proceedings of the 7th International Conference on Shock & Impact Loads on Structures (pp. 241-250). https://doi.org/10.1260/2041-4196.6.3.439

[7] Teng, T. L., Chu, Y. A., et al. (2007). Design and implementation of a high-velocity projectile generator. Combustion, Explosion, and Shock Waves, 43, 233-240. https://doi.org/10.1007/s10573-007-0033-2.

[8] Johnson, K. (1985). Contact Mechanics. Cambridge: Cambridge University Press. https://doi.org/10.1017/CBO9781139171731.

[9] Griffin, K. (1961). Impact: The Theory and Physical Behaviour of Colliding Solids.W. Goldsmith. Arnold, London. 1960. 379 pp. Diagrams. 90s. The Aeronautical Journal, 65(606), 443-443. https://doi.org/10.1017/S0368393100074861.

[10] Robins, B. (1742). New Principles of Gunnery.

[11] Johnson, R. C. (1952). The Behavior of Reinforced Concrete Slabs Under Concentrated Loads. Proceedings of the American Concrete Institute, 48(3), 485-509.

[12] Willam, J., Kossack, W. (1958). Dynamic Response of Reinforced Concrete to Impact Loading. Proceedings of the American Concrete Institute, 54(6), 803-820.

[13] Chang, W. (1981). Impact of Solid Missiles on Concrete Barriers. Journal of the Structural Division, 107(2), 257–271. https://doi.org/10.1061/jsdeag.0005640.

[14] Hughes, G. (1984). Hard missile impact on reinforced concrete. Nuclear Engineering and Design, 77(1), 23–35. https://doi.org/10.1016/0029-5493(84)90058.

[15] Haldar, F., Miller, A. (1982). "Penetration Depth in Concrete for Non Deformable Missiles," Nucl. Eng. Des., vol. 71, pp. 79–88.

[16] Haldar, A. (1985). Energy-Balanced Approach to Evaluate Local Effects of Impact of Non-Deformable Missiles on Concrete Structures. In Trans. Int. Conf. Struct. Mech. React. Technol., Volume J (pp. 209-214).

[17] Mak, L., Sicking, K. (2001). Improving Roadside Safety by Computer Simulation. Public Roads, 64(4).

[18] García, R., Triguero, R. (2019). Experimental and numerical investigation of the impact of a ship on a rigid wall. International Journal of Impact Engineering, 125, 99-113.

[19] Liu, J., Li, B., et al. (2017). Experimental and numerical investigation of the dynamic response of concrete-filled steel tubular (CFST) members subjected to impact loading. Engineering Structures, 151, 464-478.

[20] Smith, J., Johnson, A. (2018). "Impact Resistance of Normal Strength Concrete in Structural Design." Journal of Structural Engineering, 44(3), 267-279.

[21] Hammoud, A., Yan, J., et al. (2021). Blast behavior of columns built with high-strength concrete and Grade 690 MPa high-strength reinforcement. Canadian Journal of Civil Engineering, 48(11), 1422-1439. https://doi.org/10.1139/cjce-2019-0554.

[22] Lee, C., Kim, H. (2021). "Enhancing Impact Resistance through Ultra-High Strength Concrete." Concrete and Structures, 53(9), 1123-1137

[23] Daudeville, L., Malécot, Y. (2011). Concrete structures under impact. European Journal of Environmental and Civil Engineering, 15(sup1), 101-140. https://doi.org/10.1080/19648189.2011.9695306.

[24] Fang, Q., Wu, H. (2017a). Concrete structures under projectile impact. In Concrete Structures under Projectile Impact. https://doi.org/10.1007/978-981-10-3620-0

[25] Kennedy, P. (1976). A review of procedures for the analysis and design of concrete structures to resist missile impact effects. Nuclear Engineering and Design, 37(2), 183–203. https://doi.org/10.1016/0029-5493(76)90015-7

[26] Hutchings, M. (1983). Behaviour of metals under ballistic impact at subordnance velocities. Sagamore Army Materials Research Conference Proceedings, 161-196. https://doi.org/10.1007/978-1-4613-3787-4_8.

[27] Chen, W., Li, M. (2004). Transition from Nondeformable Projectile Penetration to Semihydrodynamic Penetration. Journal of Engineering Mechanics, 130(1), 123–127. https://doi.org/10.1061/(asce)0733-9399(2004)130:1(123)

[28] Alekseevskii, V. (1966). Penetration of a rod into a target at high velocity. Shock Waves.

[29] Birkhoff, G., MacDougall, D., et al. (1948). Explosives with lined cavities. Journal of Applied Physics, 19(6), 563–582. https://doi.org/10.1063/1.1698173

[30] Hazell, P.J. (2015). Armour Materials, Theory, and Design. CRC Press. Chapter 4: Penetration Mechanics.

[31] Lu, Y. (2018). Impact on Reinforced Concrete Structures. In H. Altenbach, & A. Öchsner (Eds.), Encyclopedia of Continuum Mechanics (2019 ed., pp. 1309-1332). Springer. https://doi.org/10.1007/978-3-662-53605-6_227-1

[32] Malvar, J., Ross, A. (1998). Review of strain rate effects for concrete in tension. ACI Materials Journal, 95(6), 609-616. https://doi.org/10.14359/418

[33] CEB (1993) CEB-FIP model code 1990. Committee Euro-International Du Beton, Redwood Books, Trowbridge, Wiltshire, UK

[34] Zielinski, J. (1984). Model for tensile fracture of concrete at high rates of loading. Post Positivesme, 14(c), 215-224.

[35] Lee, S., Kim, G., et al. (2018). Strain Behavior of Concrete Panels Subjected to Different Nose Shapes of Projectile Impact. Materials, 11(3), 409. MDPI AG. Retrieved from http://dx.doi.org/10.3390/ma11030409.

[36] Clifton, R. (1982). Penetration Resistance of Concrete. A Review. In National Bureau of Standards; Special Publication (pp. 480-545).

[37] Latif, I. Rahman, Z. (2015). Impact Energy of Hard Projectile for Local Damage of Concrete Slab. 1–27.

[38] Latif, I., & Memon, Q. B. alias. (2022). A Machine Learning Model for the Prediction of Concrete Penetration by the Ogive Nose Rigid Projectile. Applied Sciences, 12(4), 2040. MDPI AG. http://dx.doi.org/10.3390/app12042040.

[39] Latif, I., Bux, Q., et al. (2012). Impact Energy of Hard Projectile for Local Damage of Concrete Slab.

[40] Johnson, R., Holmquist, J. (1994). An improved computational constitutive model for brittle materials. 981(1), 981–984. https://doi.org/10.1063/1.46199.

[41] Kennedy, R. P. (1976). A Review of Procedures for the Analysis and Design of Concrete Structures to Resist Missile Impact Effects. Nuclear Engineering Design, 37, 183-203.

[42] Li, M., Reid, R., et al. (2005). Local impact effects of hard missiles on concrete targets. International Journal of Impact Engineering, 32, 224-284.

[43] Young, W. (1997). Penetration Equations (Report No. SAND97-2426). Albuquerque: Sandia National Laboratories.

[44] Unified Facilities Criteria. (2008). Design of Structures to Resist Accidental Explosions (UFC 3-340-02).

[45] U.S. Army Material Command (AMC) Headquarters. (1974). Engineering Design Handbook. Explosions in Air. Part 1 (AMC Pamphlet AMCP 706-181, Report No. AD/A-00381).

[46] Zukas, A., Walters, P. (1998). Explosive Effects and Applications. Springer. https://doi.org/10.1007/978-1-4612-0589-0.

[47] Hu, F., Wu, H. (2017). Impact performance of explosively formed projectile (EFP) into concrete targets. International Journal of Impact Engineering, 109, 150–166. https://doi.org/10.1016/j.ijimpeng.2017.06.010.

[48] Fang, Q., Wu, H. (2017b). Concrete structures under projectile impact. In Concrete Structures under Projectile Impact. https://doi.org/10.1007/978-981-10-3620-0.

[49] Fang, Q., & Wu, H. (2017b). Concrete structures under projectile impact. In Concrete Structures under Projectile Impact. https://doi.org/10.1007/978-981-10-3620-0.

[50] Mulligan, P., Baird, J. (2012). The effects of the flyer plate's radius of curvature.

[51] Federation of American Scientists. (2008). Explosively formed penetrators (EFPs) in Iraq and Afghanistan. Retrieved from https://fas.org/sgp/crs/natsec/RL34387.pdf.

[52] Bookout, L. A. (2011). Impact effects of explosively formed projectiles on normal and high strength concrete. Masters Theses. 6910.

[53] Jones, E., Kennedy, E., et al. (1980). Ballistics calculations of R. W. Gurney. American Journal of Physics, 48(4), 264-269.

[54] Kennedy, E. (1970). Gurney Energy of Explosives: Estimation of the Velocity and Impulse Imparted to Driven Metal (Report No. SC-RR-70-790). Sandia National Laboratories.

[55] Held, M. (1989). Fundamentals of Shaped Charges. In W. P. Walters & J. A. Zukas (Eds.), John Wiley & Sons, New York 1989, 398 pp., 84 Figs., ISBN 0-471-62172-2. Preparative Biochemistry & Biotechnology, 14(5), 220–220.

[56] Wu, C., Hu, S., et al. (2007). Experimental and numerical study on the flight and penetration properties of explosively-formed projectile. International Journal of Impact Engineering, 34(4), 648-655. https://doi.org/10.1016/j.ijimpeng.2006.06.007.

[57] Zakir, M., Li, Y., et al. (2018). Numerical study on the optimum design of explosively formed projectile. In 2018 15th International Bhurban Conference on Applied Sciences and Technology (IBCAST) (pp. 128-133). http://doi.org/10.1109/IBCAST.2018.8312213.

[58] Cardoso, D., Dias, F. (2016). Modelling the formation of explosively formed projectiles (EFP). International Journal of Impact Engineering, 93, 116–127. https://doi.org/10.1016/j.ijimpeng.2016.02.014.

[59] Hao, L., Gu, W., et al (2022). Damage of a Large-Scale Reinforced Concrete Wall Caused by an Explosively Formed Projectile (EFP). Defense Technology. https://doi.org/10.1016/j.dt.2022.11.003.

[60] Kingery, N. (1984). Air Blast Parameters from TNT Spherical Air Burst and Hemispherical Surface Burst.

[61] Biggs, J. M. (1964). Introduction to Structural Dynamics.

[62] Wessex Institute of Technology, "Short Course on Blast Effects and Analysis," 2020, no. October.

[63] Agu, O., Hameed, A., et al. (2018). Application of Shell Jetting Analysis to Determine the Location of the Virtual Origin in Shaped Charges. International Journal of Impact Engineering, 122, 175-181.

[64] Elshenawy, T., Elbeih, A., et al. (2018). Influence of target strength on the penetration depth of shaped charge jets into RHA targets. International Journal of Mechanical Science, 136, 234-242

[65] Johnson, R., & Cook, W. (1983). A constitutive model and data for metal subjected to large strains, high strain rates and high temperatures. In Proceedings of the 7th International Symposium on Ballistics (pp. 541-547).

[66] Johnson, G., Cook, W. (1985). Fracture characteristics of three metals subjected to various strains, strain rates, temperatures and pressures. Engineering Fracture Mechanics, 21(1), 31-48.

[67] Christou, A., Young, R., et al. (2012). Shock attenuation of PMMA sandwich panels filled with soda-lime glass beads: A fluid-structure interaction continuum model simulation. International Journal of Impact Engineering, 47, 48-59. [68] M.L. Wilkins. Calculations of Elastic Plastic Flow. Methods in Computational Physics 3:211-263, 1964.

[69] Urtiew, A., Hayeo, B. (1991). Parametric study of the dynamic JWL-EOS for detonation products. Fizika Goreniya i Vzryva, 27(4), 126-137.

[70] Hallquist, J. (2015). LS-DYNA Keyword User's Manual. Livermore Software Technology Corporation (LSTC).

[71] Coutinho, M. (2019). Mitigação de impactos com estruturas auxéticas impressas em 3-D.

[72] Basto, F. (2011). Explosivos de uso militar. Centro de treino em Explosivos e Contra-medidas. Polo Permanente do PM001/V.N.Barquinha. Tancos.

[73] Diedhiou, A., Sow, L. (2020) Contribution to Comparative Study of Physical-Chemical Characteristics of Diack Basalt and Bandia Limestone for Use in Railway Engineering. Geomaterials, 10, 25-34.

[74] Hong, J., et al. (2017). Numerical predictions of concrete slabs under contact explosion by modified K&C material model. Construction and Building Materials, 155, 1013-1024.

[75] Xu, M., Wille, K. (2015). Calibration of K&C concrete model for UHPC in LS-DYNA. In Advanced Materials Research (Vol. 1081, pp. 254-259). Trans Tech Publications. https://doi.org/10.4028/www.scientific.net/AMR.1081.254.

[76] Combe, U., Panteki, E., et al. (2015). Strain rate effects for spallation of concrete. In EPJ Web of Conferences.

[77] Schwer, E., Malvar, J. (2005). Simplified concrete modeling with MAT_CONCRETE_DAMAGE_REL3. In JRI LS-Dyna User Week (pp. 49-60).

[78] Cui, J., Hao, H., et al. (2017). Discussion on the suitability of concrete constitutive models for high-rate response predictions of RC structures. International Journal of Impact Engineering, 106, 202-216.

[79] Kong, X., Fang, Q., et al. (2017). Modified K&C model for cratering and scabbing of concrete slabs under projectile impact. International Journal of Impact Engineering. https://doi.org/10.1016/j.ijimpeng.2017.02.016.

APPENDICES

A. Compression test sheets for Basalt

Laboratório Materiais de Construção - AM

Compression test on concrete: EN 12390-3

Certificate number:	001	Certificate date:	05/06/2023
Testing machine:	Controls Pilot Pro		
Client:			
Reference:			
Specimen type:	Cilindro	Cement quantity [kg/m³]:	
Cement type:		Preparation date:	15/12/2022

Sample conditions:

Condition when received:		Condition at test time:	
Sampling location:		Sampling date:	15/12/2022
Preparation method:			
Specimen ID:	1		

Dimensions: a(mm) 150.00 b(mm) 150.00 c(mm) 300.00

Area [mm2]: 22500.0 Mass [kg]: 16.000 Density [Kg/m3]: 2370.4

Specimen age [dd]: 173

Load Rate [MPa/s]: 0.600 Test date: 05/06/2023

Max Load [kN]: 636.00 **Strength [MPa]: 28.26**

Failure type: Satisfactory

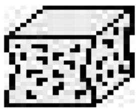

Notes:

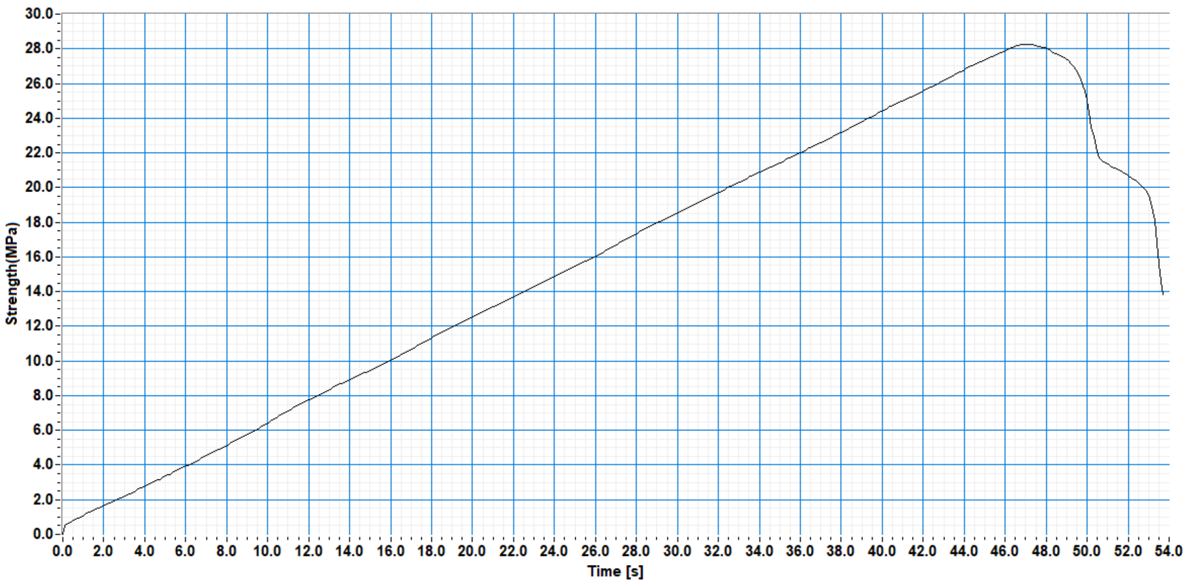

Operator:

Laboratório Materiais de Construção - AM

Compression test on concrete: EN 12390-3

Certificate number: 001 — Certificate date: 05/06/2023

Testing machine: Controls Pilot Pro

Client:

Reference:

Specimen type: Cilindro — Cement quantity [kg/m³]:

Cement type: — Preparation date: 15/12/2022

Sample conditions:

Condition when received: — Condition at test time:

Sampling location: — Sampling date: 15/12/2022

Preparation method:

Specimen ID: 1

Dimensions: a(mm) 150.00 — b(mm) 150.00 — c(mm) 300.00

Area [mm2]: 22500.0 — Mass [kg]: 16.000 — Density [Kg/m3]: 2370.4

Specimen age [dd]: 173

Load Rate [MPa/s]: 0.600 — Test date: 05/06/2023

Max Load [kN]: 751.00 — **Strength [MPa]: 33.37**

Failure type: Satisfactory

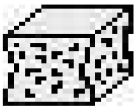

Notes:

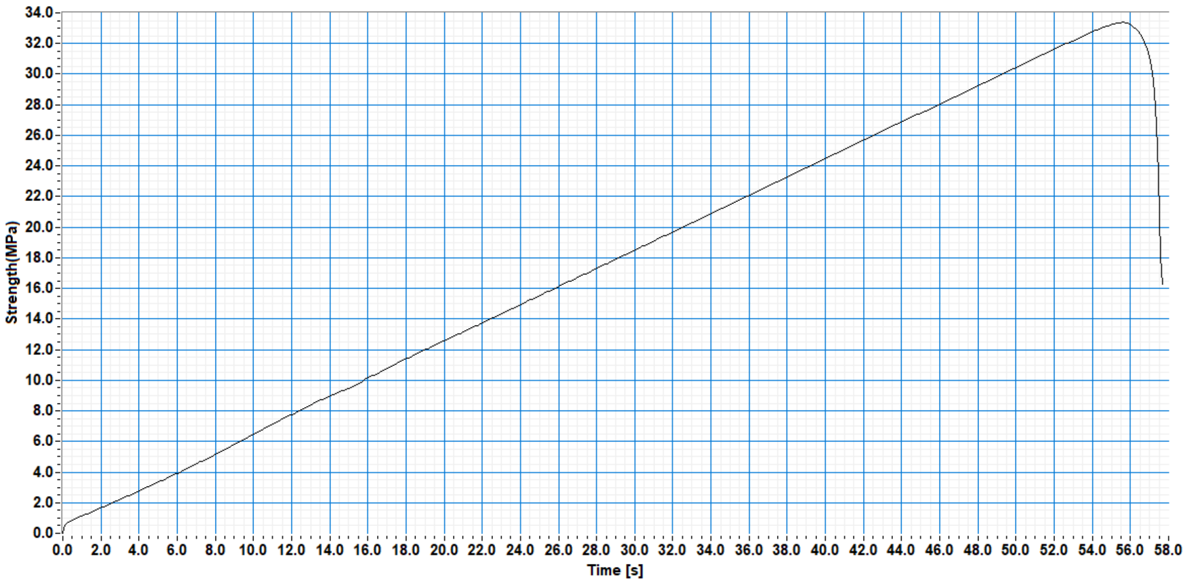

Operator:

Laboratório Materiais de Construção - AM

Compression test on concrete: EN 12390-3

Certificate number:	001	Certificate date:	05/06/2023
Testing machine:	Controls Pilot Pro		
Client:			
Reference:			
Specimen type:	Cilindro	Cement quantity [kg/m³]:	
Cement type:		Preparation date:	15/12/2022

Sample conditions:

Condition when received:		Condition at test time:	
Sampling location:		Sampling date:	15/12/2022
Preparation method:			
Specimen ID:	1		

Dimensions: a(mm) 150.00 b(mm) 150.00 c(mm) 300.00

Area [mm2]: 22500.0 Mass [kg]: 16.000 Density [Kg/m3]: 2370.4

Specimen age [dd]: 173

Load Rate [MPa/s]: 0.600 Test date: 05/06/2023

Max Load [kN]: 728.00 **Strength [MPa]: 32.37**

Failure type: Satisfactory

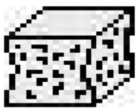

Notes:

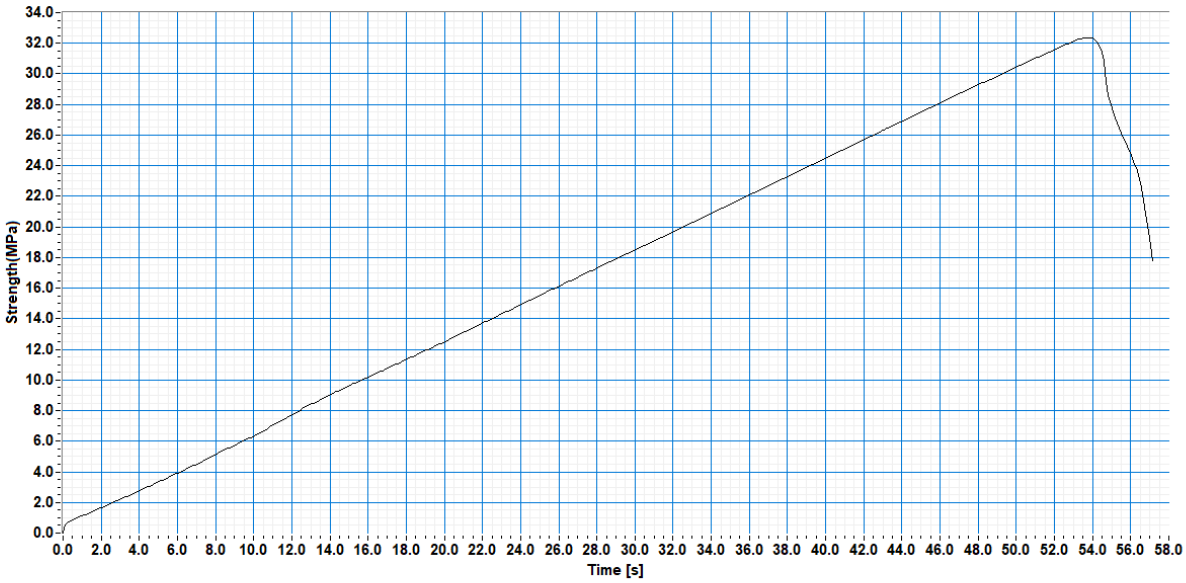

Operator:

B. Compression test sheets for Limestone

Laboratório Materiais de Construção - AM

Compression test on concrete: EN 12390-3

Certificate number: 001 | Certificate date: 15/12/2021

Testing machine: Controls Pilot Pro

Client:

Reference:

Specimen type: Cilindro | Cement quantity [kg/m³]:

Cement type: | Preparation date: 08/02/2022

Sample conditions:

Condition when received: | Condition at test time:

Sampling location: | Sampling date: 15/12/2022

Preparation method:

Specimen ID: 1

Dimensions: a(mm) 150.00 b(mm) 150.00 c(mm) 300.00

Area [mm2]: 22500.0 Mass [kg]: 16.000 Density [Kg/m3]: 2370.4

Specimen age [dd]: 165

Load Rate [MPa/s]: 0.600 Test date: 05/06/2023

Max Load [kN]: 663.00 **Strength [MPa]: 29.45**

Failure type: Satisfactory

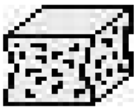

Notes:

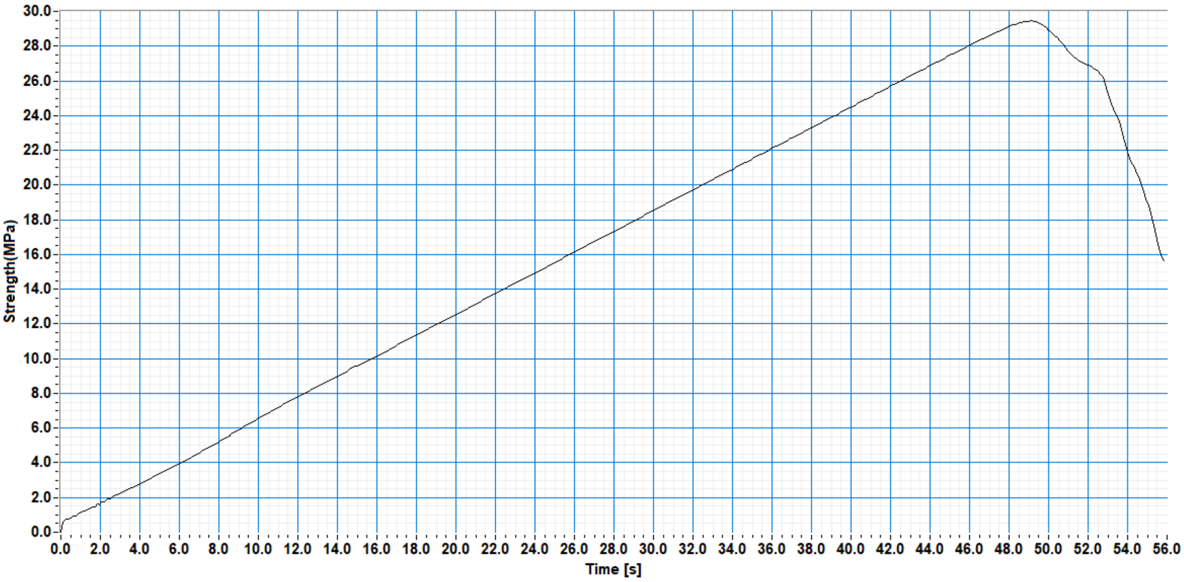

Operator:

Laboratório Materiais de Construção - AM

Compression test on concrete: EN 12390-3

Certificate number: 001 Certificate date: 05/06/2023

Testing machine: Controls Pilot Pro

Client:

Reference:

Specimen type: Cilindro Cement quantity [kg/m^3]:

Cement type: Preparation date: 15/12/2022

Sample conditions:

Condition when received: Condition at test time:

Sampling location: Sampling date: 15/12/2022

Preparation method:

Specimen ID: 1

Dimensions: a(mm) 150.00 b(mm) 150.00 c(mm) 300.00

Area [mm2]: 22500.0 Mass [kg]: 16.000 Density [Kg/m3]: 2370.4

Specimen age [dd]: 173

Load Rate [MPa/s]: 0.600 Test date: 05/06/2023

Max Load [kN]: 573.00 **Strength [MPa]: 25.47**

Failure type: Satisfactory

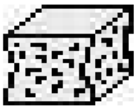

Notes:

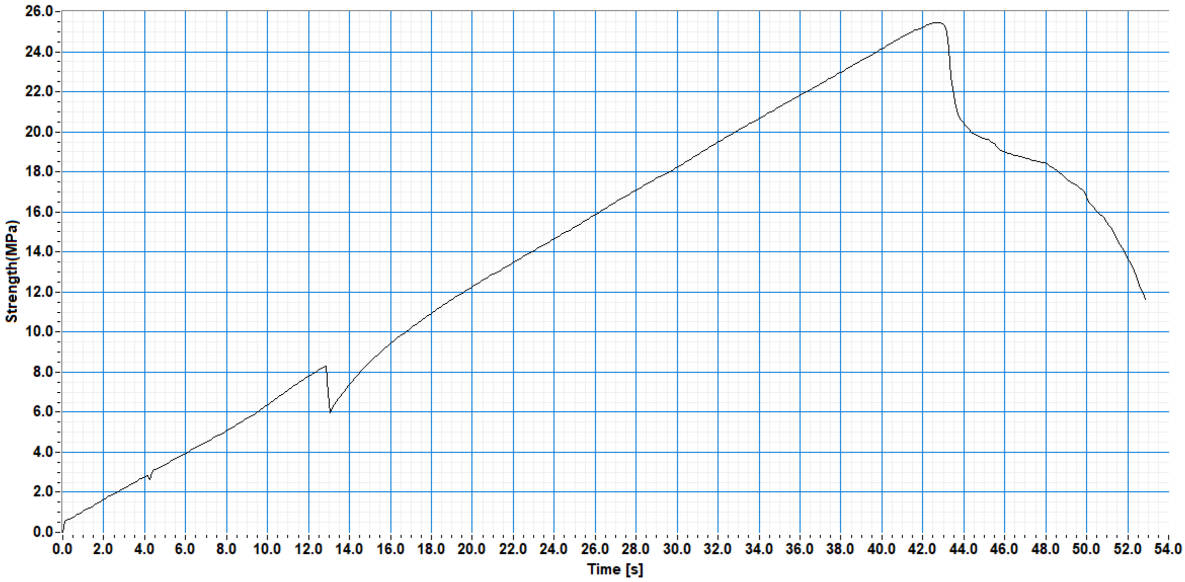

Operator:

Laboratório Materiais de Construção - AM

Compression test on concrete: EN 12390-3

Certificate number: 001

Certificate date: 05/06/2023

Testing machine: Controls Pilot Pro

Client:

Reference:

Specimen type: Cilindro

Cement quantity [kg/m^3]:

Cement type:

Preparation date: 08/02/2023

Sample conditions:

Condition when received:

Condition at test time:

Sampling location:

Sampling date: 15/12/2022

Preparation method:

Specimen ID: 1

Dimensions: a(mm) 150.00 b(mm) 150.00 c(mm) 300.00

Area [mm2]: 22500.0

Mass [kg]: 16.000

Density [Kg/m3]: 2370.4

Specimen age [dd]: 165

Load Rate [MPa/s]: 0.600

Test date: 07/06/2023

Max Load [kN]: 729.00

Strength [MPa]: 32.41

Failure type: Satisfactory

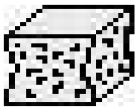

Notes:

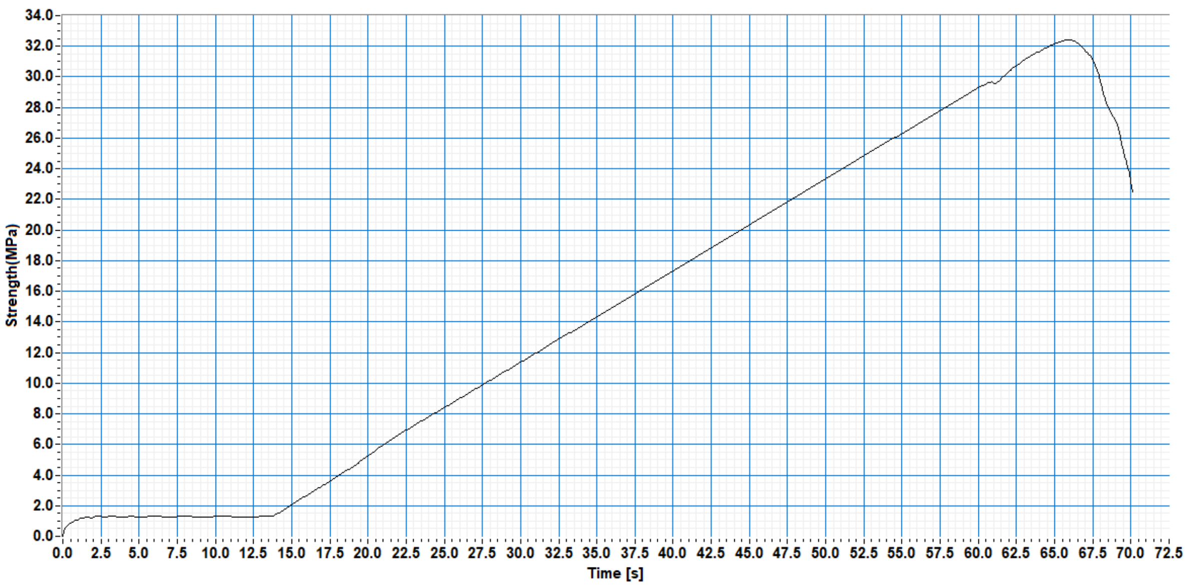

Operator: